Investigation of the Characteristics of an Axisymmetric Jet Subjected to Azimuthal Forcing

by

Arthur Weiner

A thesis submitted to the Graduate Faculty of
Auburn University
in partial fulfillment of the
requirements for the Degree of
Master of Science

Auburn, Alabama
August 03, 2013

Keywords: Axisymmetric round jet, Azimuthal forcing, Strouhal number, PIV, POD, Hot wire anemometry

Approved by

Anwar Ahmed, Chair, Professor of Aerospace Engineering
Roy Hartfield, Walt and Virginia Woltosz Professor of Aerospace Engineering
Jay Khodadadi, Alumni Professor of Mechanical Engineering

Abstract

Characteristics of an axisymmetric jet subjected to azimuthal forcing were investigated. A circular variable diameter iris was positioned near the nozzle exit to impart azimuthal excitation to the jet at desired Strouhal numbers. The experiments were conducted at the Reynolds number of $5,500$. Two excitation frequencies corresponding to the Strouhal number of 0.12, and 0.09 were used. It was found that both excitation frequencies attenuated the large scale structures in the near-field of the jet, however, the harmonic forcing introduced low frequency instabilities within the first two diameters of the nozzle exit plane. The harmonic forcing also introduced more energy into the flow than the sub-harmonic forcing and was evident from the distribution of the turbulent kinetic energy, power spectral density, and visualization of the instabilities. The forcing also had an effect on the streamwise vortex filaments located between successive large-scale structures of the jet. The diameter of the streamwise vortex filaments and meandering increased for both forcing cases. The filaments played a pivotal role in the entrainment of ambient fluid and the distortion of the vortices due to additional strain.

Table of Contents

List of Figures

List of Tables

<center>Nomenclature</center>

$A,\ B$ Experimental constants

C Correlation Matrix

$C_o \ldots C_4$ Experimental constants

D Nozzle Diameter

E_{AD} A/D board input range

U Velocity

U_c Centerline Velocity

U_{max} Maximum velocity at nozzle exit

f Frequency

$f_{cut-off}$ Cut off frequency

m Resolution in bits

n Number of snapshots

t_{record} Data record length

$u',\ v'$ Velocity fluctuation

x Eigenvector

Re   Reynolds number based on jet diameter

St   Strouhal number

<center>x</center>

TKE	Turbulent kinetic Energy
δ_d	Displacement thickness
δ_m	Momentum thickness
$\frac{\partial U}{\partial E}$	Slope or sensitivity factor
λ	Eigenvalue
μ	Dynamic Viscosity
ρ	Density
σ	Standard deviation, in percent
τ_{xy}	Reynolds shear stress

Chapter 1

Introduction

Mixing enhancement has been a subject of research for the last several years as it involves the entrainment of surrounding fluid and rapid spreading of a jet. Combustor efficiency, ejectors, noise attenuation etc. are a few applications where mixing enhancement is desirable. Controlling the mixing characteristics of a jet is essential to maximizing the performance of a nozzle for the given application [3]. Fuel and air mixing at the molecular level is important for combustion efficiency and actuators offering significant mixing in the small scale [4].

Excited laminar jets were first described by Leconte and Tyndall in 1867, they noted the gas flames responded to the music in a synchronized manner. Tyndall studied this phenomenon by using a series of flame tubes with different apertures and concluded that the sound led the flame to transition to turbulence [5].

In 1933, Schlichting developed a model for a high Re laminar jet. Realistically, a high Re laminar jet cannot exist because instabilities result in the appearance of turbulence. He, however, concluded that the momentum of the jet remained constant with downstream distance and that the mass flow continually increased [6].

Crow and Champagne were the first to quantify the patterns of a round turbulent jet and attempted to control the jet through periodic forcing. They studied a round axisymmetric jet using a water and air facility. They visualized jet instabilities as the flow evolved from a sinusoid, to a helix, and finally a train of axisymmetric waves as Re increased from 10^2 to 10^3 [7].

1.1 Coherent Structures in Jet Mixing

Several early studies focused on the mixing layer [1] [8] [9]. It was originally thought that the measured fluctuations of the flow were random and could only be addressed statistically. By the 1960's some researchers began to postulate that the fluctuations were not entirely random. In 1971, Lau et al proposed a model to explain the phase relationships and fluctuating velocity in the mixing layer. They believed that underlying structures in the mixing layer could affect other regions of the jet and conducted hot wire and microphone measurements in the potential core and entrainment regions. Their analysis showed that there was a semi-regular array of vortices. Lau verified and concluded by changing the jet velocity that spectral peaks should be located at the fundamental frequency [10] [11].

The work by Crow and Champagne is considered as fundamental in the study of turbulent mixing and the frequency spectra within a jet. Using flow visualization methods to study jets at the Reynolds number range of 10^2 to 10^5, they noticed that as Re increased the flow transitioned to turbulent and a series of large-scale vortex "puffs" formed downstream with an average Strouhal number of 0.3. They also discovered that acoustic excitation of the jet at the average Strouhal number (0.3) resulted in the largest amplification downstream of the vortex puffs ("rings") [7]. Due to their work, orderly structures became known as "coherent structures." Fiedler clarified the definition of coherent structures as dominant patterns that can usually be recognised in a flow [9].

Subsequent researchers studied coherent structures based on qualitative data in the form of flow visualizations rather than quantitative data [7] [12] [13]. While advances were made from the qualitative interpretations there was an inherent level of bias, predominately on the viewer. The availability of newer optical diagnostic techniques and data analysis techniques, such as POD, have become more suitable to obtaining quantitative data of coherent structures [14] [15] [16] [17] [18].

1.2 Modes and Stability

In an axisymmetric round jet, the initial wave at the nozzle exit is similar to a Kelvin-Helmholtz instability that occurs when a perturbation is introduced between two inviscid flows. As these structures move downstream they grow rapidly, coalesce, and become chaotic [19]. Downstream, the instabilities amplify and non-linear effects become more pronounced.

In axisymmetric flows there are three common modes of symmetry: the ring, helix, and double helix [9] and they correspond to the 0th, 1st, and 2nd modes. The initially most unstable mode is the axisymmetric (ring) mode and this is usually due to the geometric symmetry of the jet. As the distance downstream increases, the antisymmetric (helix) mode becomes more prominent [20].

A dimensionless parameter (Strouhal number), which describes the flow mechanisms, is commonly used to express the preferred mode or most amplified frequency and typically the Strouhal number increases with the Reynolds number. According to Crow and Champagne, the preferred mode occurred at a $St = 0.3$ [7].

1.3 Characteristics of an Axisymmetric Round Jet

Unlike the plane jet that can be statistically considered two-dimensional [21] , a round jet is not completely two-dimensional this is due to the large eddies that contain a majority of the turbulent energy [1] .

The jet is borne out of the nozzle exit plane and it entrains the quiescent fluid creating a velocity shear between the quiescent and entering fluid. The flow spreads in the lateral direction with increasing downstream distance until the initial momentum is spread out in the fully developed far field or the jet reaches a state of self-similarity.

The initial region of a round jet is characterized by a laminar shear layer shown just downstream the nozzle exit plane in Figure 1.1. The initial instability modes are dependent on the nozzle exit conditions and produce the flow structure in the shear layer. A good

example of this was studied by Reynolds who produced bifurcating and blooming jets [22]. The instabilities typically grow rapidly due to the unstable nature of the shear layer and form ring vortices that carry the turbulent fluid into the ambient fluid. The viscosity also helps to initialize the roll-up in the mixing layer and creates a three-dimensional instability [8]. The intensity of the vortex pairing is also dependent on initial conditions. Vortex pairing is a naturally occurring event where the trailing vortex is pulled through the leading ring similar to a "leap frog" motion. This motion increases the radius and decreases the strength of the vortex which in turn makes it more susceptible to instabilities in the azimuthal direction. Vortex pairing is indicated by the arrows in Figure 1.2.

The velocity profile is determined by nozzle geometry. A smooth contraction nozzle produces a top hat velocity profile and a sharp-edge nozzle produces a saddle-backed initial velocity profile.
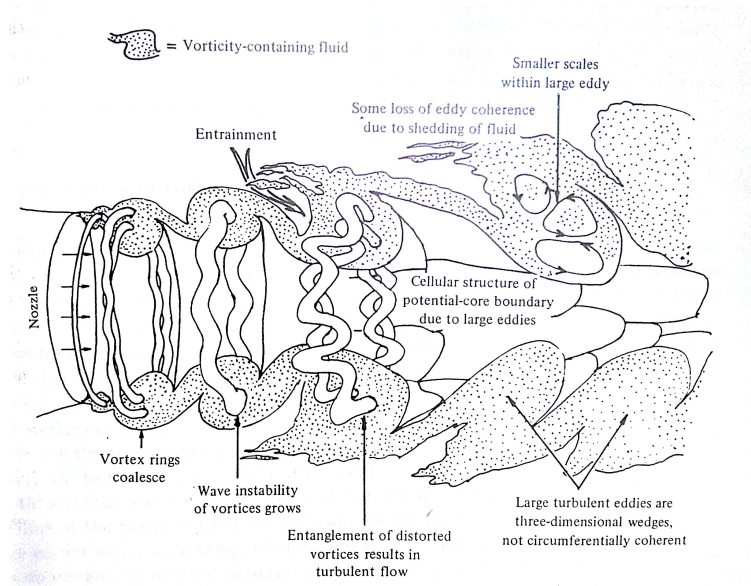

Figure 1.1: Physical structure of a transitional jet [1]

There are three regions located within a round turbulent jet. The *near field*, *far field*, and *transitional region*. The near field is defined as the area where the flow characteristics match the nozzle exit and encompasses the potential core. The near field usually extends
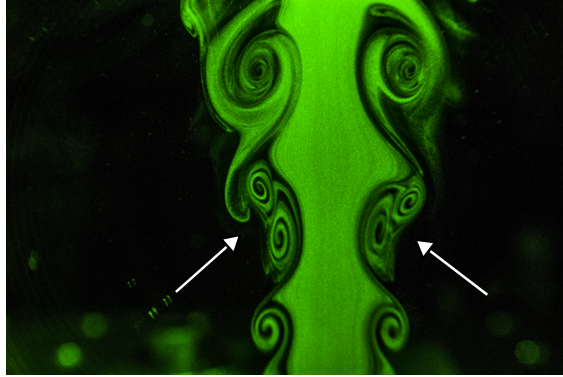
Figure 1.2: Vortices coalescing

to six to seven diameters downstream. This can be seen in Figure 1.1 before the vorticity-containing fluid region engulfs the jet flow.

The far field is located roughly $y/D > 70$ where the flow is fully-developed and considered to be in equilibrium. The classical self-similarity view is that this state depends only on the rate of momentum addition and is independent of other initial conditions [23]. In other words, the influence on the flow due to the initial conditions decays rapidly with downstream distance and is eventually eliminated. Recently, there has been confusion to whether the scalar fields are universal. Pitts and Richards found that there is a $\pm 15\%$ variation in spreading rate [24]. Typically the variations have been attributed to experimental error or differences in experimental conditions or apparatus [25]. George conjectured that there are multiple self-similar states for a particular flow and the initial conditions will uniquely define the states [26]. Thus, the entire flow is influenced by the initial conditions. The work by George was confirmed by Mi who concluded that the turbulent properties throughout the flow do depend upon the initial conditions [23].

Also within this region, the energy spectrum is found to exhibit a $-5/3$ exponent [27], similar to Kolmogorov's $-5/3$ law.

The transitional region is located between the two. Here, the vortex rings that were created near the nozzle exit due to the shear layer become three-dimensional. In addition to

the vortex rings, streamwise structures have been found between successive vortex cores in the shear layer (known as "braids") [8].

1.4 Methods of Mixing

There are two distinctive methods of jet excitation, active and passive. Both active and passive have been employed to modify the spreading and turbulence characteristics of jet flows. Active techniques add energy at an appropriate frequency and amplitude. Some active methods studied were fluidic actuators, blowing, acoustic actuators, and synthetic jets. Passive techniques work by modifying the critical conditions such as nozzle exit conditions or the introduction of objects into the flow to alter the development. Passive techniques include tabs mounted to the jet exit, non-circular shaped nozzle, adding a ring or mesh to the nozzle exit or a specific distance downstream from the nozzle.

1.4.1 Tabs and Blowing

Use of tabs and blowing are passive and active mechanisms, respectively. However, the two forcing designs typically go hand-in-hand therefore they are combined in this section. Tabs effectively increase the spread rate by obstructing the flow via streamwise vorticity.

Samimy et al studied the effect of tabs and blowing on jets ranging from mach number $M = 0.3 - 1.81$. They acknowledged that for subsonic jets the effects of tabs was more pronounced than that produced by other mixing enhancement techniques. Through schlieren photography they visualized the formation of a pair of counter-rotating streamwise vortices that shed from the tabs[28] and speculated that the tabs act more similar to wing tip vortices and that the streamwise vorticity was pressure driven and inviscid phenomenon [28].

1.4.2 Acoustic Drivers

For many years, acoustic drivers were the preferred method of exciting jets because of the availability and the highly controllable nature of the drivers at a wide range of frequencies. Acoustics drivers are ideal for laboratory experimentation where the fundamental understanding of the flow is principal. However, they are not well suited for exciting high Re flows as the low amplitude perturbations are drawn out due to the turbulent fluctuations within the flow. Therefore, high amplitude fluidic actuators became popular for jet mixing applications.

Recently Aydemir et al used speakers located in the plenum chamber to acoustically excite a round jet. The design provided large-amplitude acoustic forcing with sinusoidal oscillations that resulted in the high-amplitude forcing initiated the shear layers of the jet to break-up into a series of large scale vortex rings [29]. The size and spacing between consecutive vortex rings remained dependent on the amplitude and frequency of the forcing conditions.

1.4.3 Synthetic Jets

Over the last decade synthetic jets have been gaining popularity for the purpose of jet mixing. Synthetic jets use a power and recovery stroke to suck in and blow out equal amounts of ambient fluid resulting in a zero mass flow. Synthetic jets tested to date either use a piston cylinder device or piezoelectric ceramics. Piezoelectric ceramics were initially used to detect structural deformation [30], however, due to their properties when an electric field is applied a proportional deformation is achieved [31]. These ceramics are mounted on flexible plates and serve as diaphragms are typically located in the plenum chamber, in a cavity near the jet exit [32] [33]. Typically, ceramics produce lower amplitudes when excited. The amplitude is also restricted to the high frequencies (mostly resonant) that the ceramics are driven at. An advantage of high frequency actuators is that small scale fluctuations can more easily be excited [4] [34].

Pothos and Longmire studied rectangular jets excited with a synthetic jet actuator located on one wall. The jet was run at $Re = 4240$ and excited at $St = 0.25$, 0.42, and 1.46. They found that forcing at the lowest frequency increased the centerline velocity decay as well as spreading rates in the far field. They concluded that the effects of forcing at $St = 1.46$ were nominal and the disturbances were quickly attenuated [33].

1.4.4 Passive Techniques

Unlike active methods, passive techniques depend on modifying critical conditions. These conditions are typically exit conditions or introducing an obstruction into the flow. An advantage of passive techniques are that they do not require an external energy source.

Mi et al [3] designed a self-exciting nozzle to analyse the mixing characteristics of a low-frequency flapping jet. Here the "flapping" is described as the two-dimensional flip-flop motion of the entire jet with respect to the major plane of symmetry of the inner nozzle . This form of excitation enhances the large-scale mixing and suppresses fine scale turbulence generation. However, the large-scale oscillations decayed rapidly and were not captured in the far field. They also found that the large scale turbulence suppressed the small scale mixing downstream of the nozzle.

Parker and Rajagopalan used a thin wire ring to alter the flow and placed a 0.5 mm wire at $x/D = 0.15$ and found that adding a thin ring axisymmetrically in the mixing layer improved the similarity throughout the mixing layer [35]. They also found significant reductions in both, the RMS axial and radial velocity fluctuations (22% and 15%, respectively)

1.5 Objectives

Previous studies on the excitation of jets have focused on discrete locations for the forcing, however even for the unforced jet, secondary flows in the form of jet blooming ([22]) have been reported. The location of blooming and preferred location of the onset of instabilities, although attributed to imperfections in the nozzle, remains to be investigated.

The primary objective of the present work was to perturb the jet in a novel manner that ensured continuous forcing along the outer periphery of the jet near the origin of the shear layer and to study the spatial growth of instabilities along the axis of the jet.

Chapter 2

Experimental Set-up

Experiments were performed in the Vortex Dynamics Lab at Auburn University. A flow conditioner consisting of honeycomb and serveral screens was designed for low turbulence flow at the exit of a smooth contoured nozzle. A mechanical forcing mechanism was designed to azimuthally force the flow at 360°. Due to the design of the mechanism (Figure 2.1) there was a slight rotation in the leaves as the aperture diameter changes. The mechanism also needed to provide fluidic motion at the nozzle exit in the form of a square wave.

Figure 2.1: Isometric view of the iris

2.1 Turbulent Jet Facility

The jet facility consists of a vertical, cylindrical plenum chamber with an internal diameter of '5 in and a length of 18 in. A Dayton Electric Company DC blower supplied air to

the chamber. A series of fine mesh and 2 *in* thick honeycomb are located in the flow conditioning chamber to eliminate swirl and achieve uniformity. The nozzle with an exit diameter of 0.5512 *in* was machined from aluminium with a smoothly contoured inner profile to give a top-hat exit velocity profile. The jet exit velocity was varied by varying the pressure in the plenum chamber. A total pressure probe was machined in the wall of the plenum chamber for calibration purposes.

2.1.1 Probe Traversing System

A two axis traverse was designed to vary the location for single point measurements and allowed measurements to be taken up to $20D$ downstream. The traverse was affixed to an optical table that was aligned with the jet. Figure 2.2 shows the set-up used for single point measurements. The two stepper motors at the end of the traverse are controlled by a Velmex NF90 stepper motor controller that was connected to a PC. A customized LabVIEW program was written to control the streamwise and lateral traversing distance and resolution with a high level of spatial accuracy for velocity measurements.

2.2 Forcing Mechanism

A limited angle high torque brushed motor from H2W Technologies, Inc., model TMR-060-005-2H, was used for forcing mechanism as the air jet was pressed through an optical iris consisting of 16 leaves. A schematic of the forcing mechanism is seen in Figure 2.3.

The brushed motor was driven by an AMC DigiFlex Servo drive, DZRALTE-020L080 and mounted on an MC1XDZR02-QD mounting card. Block diagrams for the set-ups are found in Appendix B.3 and B.4, respectively. The digital servo drive was selected as it offered optimal performance for brushed motor, and included encoder feedback, and ran smoothly with DriveWare software. A rotary encoded purchased from US Digital and used to send feedback information of the motor shaft. Software developed by AMC, DriveWare 7.0.2, was

used to control the motor. Within the software, the current, position, and velocity loops were tuned to minimize the residual in the target and measured waveform.
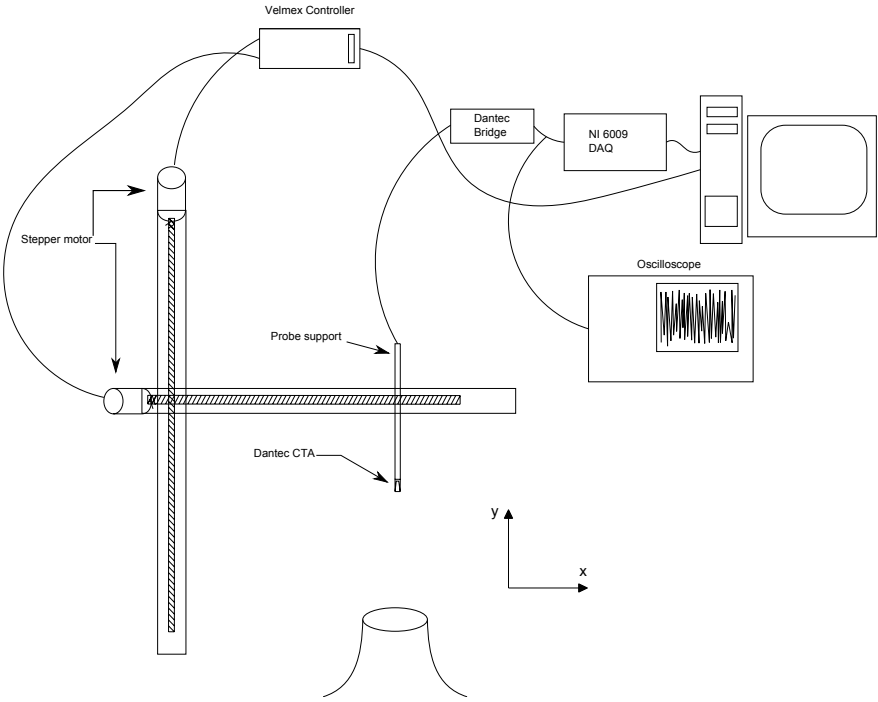

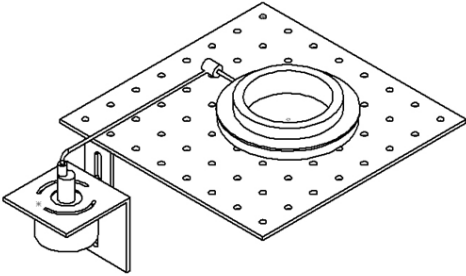Figure 2.2: Experimental setup with probe traverse and data acquisition system

Figure 2.3: Isometric view of the forcing mechanism

2.3 Hot Wire

The technique of constant temperature anemometry (CTA) works through the heat transfer from a wire to the surrounding fluid. By using thin wire sensors and a closed loop system it is possible to measure fine velocity fluctuations within a flow.

Hot wire anemometry can measure flow velocities in up to three separate directions. This is accomplished by a single, dual, triple wire sensor. Single wire sensors measure one component (U), dual and triple measure two (U and V) and three (U, V, W) components. Each sensor offers its advantages and disadvantages based on application.

While CTAs have been around for many years and they still compete with non-intrusive optical diagnostic techniques such as particle Image Velocimetry (PIV). Also, no information is lost while collecting data because output data is a continuous analogue voltage. This also allows anlysis of the data for turbulence statistics and spectral analysis. CTA also has a very high frequency response (≈ 100 kHz).

While dual and triple wire sensors can collect data in multiple directions they also increase experimental error due to the disturbances induced by additional wires [21]. This error is small and usually accounted for within the *in situ* calibration. This method, however, is an intrusive technique and can modify the local flow field. There can also be errors in the calibration due to neglecting higher order terms and the wires can be insensitive to reversal in the flow direction [36]. The sensors are also fragile and prone to breaking and burn out.

2.3.1 Circuit

The CTA utilizes a Wheatstone bridge, servo amplifier, and voltage source as seen in Figure 2.4. The probe that is exposed to the flow is added to one arm of the Wheatstone bridge and opposite to a variable resistor ($R3$). This resistor defines the operating resistance and temperature of the circuit. While the bridge is balanced, there is not a voltage potential across the circuit. As the flow velocity increases, the wire resistance will decrease. The servo

amplifier within the closed loop will increase the current within the probe. This will continue until the balance is restored within the bridge.
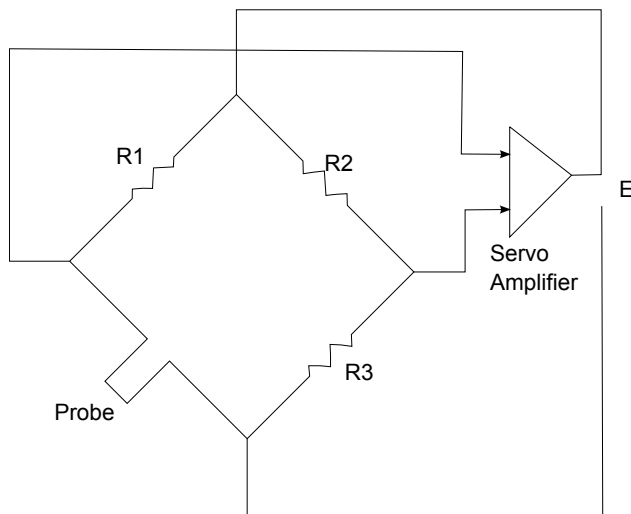

Figure 2.4: The circuit for the CTA bridge

The setup of the anemometer is crucial to ensuring accuracy of the data collected and minimizing erroneous frequencies. The set-up consists of a signal conditional. It is important to apply a high and/or low pass filters to "clean" the signal. A low pass filter is used to remove noise and to prevent higher frequencies from folding back (aliasing). If a low pass filter is not utilized, the energy at frequencies $<f_{cut-off}$ can be contaminated by higher frequencies. The $f_{cut-off}$ frequency is typically calculated using the Nyquist criteria. A high-pass filter is typically used when a Fast Fourier transform (FFT) is required. When the CTA signal fluctuates on a time-scale longer than the total length of the data record, it will give an unwanted high frequency contribution in the FFT-based spectrum. Otherwise it should not be applied [37]. The $f_{cut-off}$ frequency for the high-pass filter is found by

$$f_{cut-off} = \frac{5}{2t_{record}} \qquad (2.1)$$

This eliminates waves with a wavelength larger than 2/5 of the record length. If there are oscillations larger than the total length of the data it can give unwanted high frequency contributions. High pass filter makes the signal stationary by it eliminates low-frequency oscillations. Therefore, in some cases digital filtering using software such as MATLAB may be favourable.

2.3.2 Calibration

The use of a CTA is a relative technique so it must be calibrated *in situ* against a known flow velocity. The calibration was performed by exposing the hot wire probe to a set of known velocities U to the corresponding voltage E. A curve fitted through the acquired data is used for the calculation of velocity. Typically, the calibration is carried out with a low turbulence free jet or in a wind-tunnel. For the present research, the round jet was used for the calibration.

To calculate the known velocities, a total pressure port was placed in the plenum chamber and connected to a transducer to calculate the velocity at the nozzle exit are the same. Once the output voltage, E, from the CTA and corresponding velocity, U, were determined a relationship can be found. Perry discusses two methods for finding the relationship between U and E for hot wire calibrations [38]. The Kings' Power Law, given by

$$E^2 = A + BU^n \tag{2.2}$$

Here n is a numerical constant usually taken to be 0.45 for most hot wires [21]. The polynomial curve fit, given by,

$$U = C_o + C_1 E + C_2 E^2 + C_3 E^3 + C_4 E^4 \tag{2.3}$$

For the present research the polynomial fit was chosen. It is important to note that the polynomial fit is not a good representation if the range of velocities does not lie within the calibrated range.

2.3.3 Data Acquisition

The CTA probes were mounted vertically through a custom designed aluminium mounting bracket to the traverse located perpendicular to the flow direction as seen in Figure 2.2. This bracket was capable of holding both single and double sensor probes. Hot wire anemometry requires a data acquisition system. The single wire CTA probe was connected through a coaxial cable to a Dantex Dynamics MiniCTA 54T30. The system consisted of a built-in signal conditioner and dip switches to account for the operating resistance. Since the raw data consists of an analogue signal, and a National Instruments USB-6009 A/D data acquisition with a 48 kHz multi-channel A/D converter with a 12-bit resolution. The signal was originally monitored with a Hitachi V-1060 oscilloscope. Real time data was acquired via a customized LabVIEW program and analyzed using Matlab.

2.4 X-Wire

The X-wire calibration and procedure are similar to the single wire. However, the data acquisition system was designed by TSI. CTA probes are available with different type of sensors, commonly miniature, gold-plated wire, fibre-film or film-sensors. Most wires are $5\,\mu m$ in diameter and 1 to $2\,mm$ in length, suspended between two needle shaped prongs [37]. The probes for this study were developed by Dantec Dynamics and are $5\,\mu m$ diameter and are $2\,mm$ in length. The experimental set-up can be seen in Figure 2.5, with the only difference being that instead of a matrix board of BNC connectors a PD2-MFS-4-2M/14 PCI board from United Electronics Industries (UEI) was used. This PCI board has 4 single-ended simultaneous sample A/D channels with 14-bit resolution and 4 MHz sampling rate.
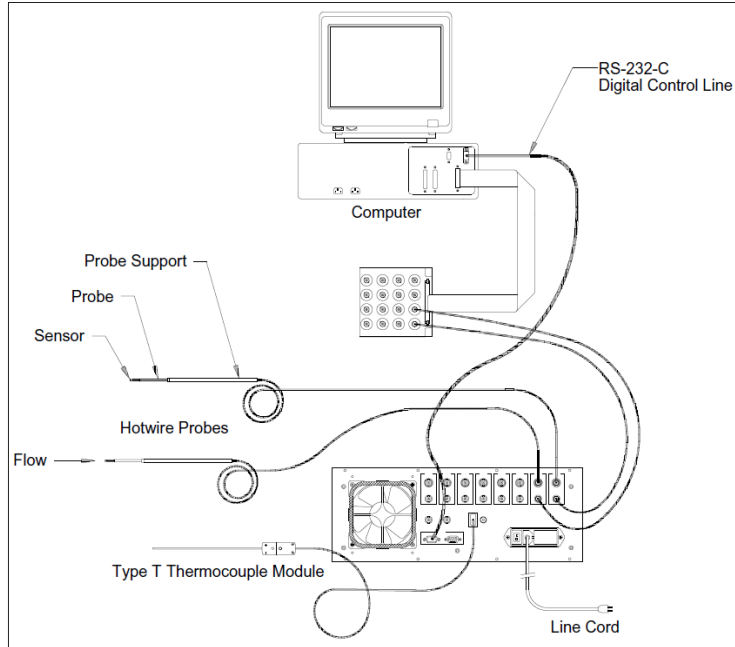
Figure 2.5: Overview of the IFA300 set-up[2]

Signal conditioning, calibration, and data acquisition was conducted through the IFA 300 system. The TSI IFA 300 system developed by TSI non-dimensionalizing the turbulent quantities by the local mean velocity. Interested in global turbulent field, a custom Matlab code was written to analyse the output velocity text files. Unless otherwise specified, all scalar fields presented were non-dimensionalized by the maximum velocity. The custom code also allowed scalar quantities that were previously not calculated within the IFA algorithm to be included.

2.5   Particle Image Velocimetry

Another method commonly used to analyze the instantaneous velocity and turbulence fields, as well as, large-scale structures within a flow is PIV. PIV is advantageous because it highlights large-scale structures at any given instant.

A New Wave Research Solo III ND:YAG dual pulse laser was used in conjunction with two mirrors and a plano-concave lens to create a two-dimensional light sheet of 1 mm thickness. To account for the larger-than-normal light sheet, the f-stop was set to the minimum allowed (3.8). The images were captured by a Cooke Corporation high speed camera with a Tamron 75 mm lens. The laser and camera were synced with two Model 9514 quantum composers. The pulse rate for each beam was set at 2 Hz and the pulse duration was varied to allow the maximum particle displacement to be 8 $pixels$. The interrogation windo was 32 by 32 pixels.

The flow was seeded with an Antari $Z-800II$ smoke generator. The mineral oil within the smoke generator was propelled through a heated nozzle that vaporized the heated oil. Smoke accumulated at the location of the blower to observe the flow along the jet centerline as well as in the ambient flow to visualize the fluid entrainment.

The images were acquired through CamWare 2.19 software and initially analyzed through Fluere version 1.3. A custom developed Matlab program was also used in conjunction with Fluere for post processing of the images.

2.5.1 Proper Orthogonal Decomposition

There are other experimental techniques used to extract coherent structures from turbulent flows however they conditional techniques. Conditional techniques involve sampling the flow at specific time intervals which is predicated on criteria that is deemed significant to the information that is sought, such as variable-interval time averaging (VITA) [16]. Lumley proposed a "non-conditional" technique of extracting eigenvectors from single point measurements to identify coherent structures within a turbulent flow [39].

For the current work, a "snapshot" POD method was applied. POD extracts a set of eigenfunctions or "modes" from a cross-correlation matrix [16]. The mathematical approach used is described below.

The POD consists of solving the eigenvalue-eigenvector equation,

$$Cx_n = \lambda_n x_n \tag{2.4}$$

This is accomplished by formulating a matrix $S = f(x, y, n)$, where n is the number of snapshots processed according to Section 2.5.1. The correlation matrix C is defined as the inner product of the velocity perturbations of S and consisted of $1,000$ images. The perturbations are found according to Reynolds decomposition. The eigenvalues can then be extracted from equation 2.4 such that

$$\lambda_1 > \lambda_2 > \lambda_3 > ... > \lambda_n \geq 0 \tag{2.5}$$

Commonly a singular value decomposition is used,

$$C = U\Sigma V^T \tag{2.6}$$

where U is an n x n orthogonal matrix, V is an m x m orthogonal matrix, and Σ is an n x m matrix with only values on the diagonal non-negative and are in the same form as equation 2.5. The rank of this matrix is n and $\lambda_{length(n)} \approx 0$.

From equation 2.5 and since the sum of all the eigenvalues gives the total turbulent kinetic energy in the flow, the first eigenvalue contains the largest amount of kinetic energy and each subsequent mode will contain a decreasing amount [14]. POD is commonly used because it is efficient at capturing the dominant components (modes) of an infinite-dimensional process with only a few functions [15].

Chapter 3

Results

Measurement were made at several streamwise and cross-stream locations measuring instantaneous velocity and consisted of turbulence statistics and spectral content. The following section contains the velocities and turbulence field characteristics due to the forcing mechanism. It is also important to note that for nondimensionalizing purposes a capital letter in the denominator corresponds to a global quantity and lower case is local.
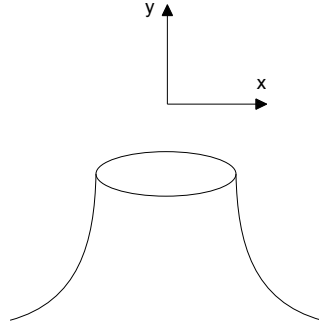
Figure 3.1: Coordinate System

The coordinate system for the jet were defined in Figure 3.1. Typically polar coordinates would characterize a round jet. However, for this research, a Cartesian coordinate system was used since the jet is axisymmetric. Therefore, the round jet has the dominant motion in the streamwise (y) direction and jet growth in the lateral or azimuthal (x) and (z) directions.

It has been established that at high Re the mean velocity profiles and spreading rates of a round jet are nearly independent of Re and at sufficiently low Re ($Re < 10,000$), both the mean and turbulence field are dependent on Re [21] . Therefore, test were conducted at $Re = 5,500$ where Reynolds number was calculated from,

$$Re \quad = \quad \frac{\rho V D}{\mu} \qquad (3.1)$$

(a) Velocity Profile   (b) Turbulent Intensity
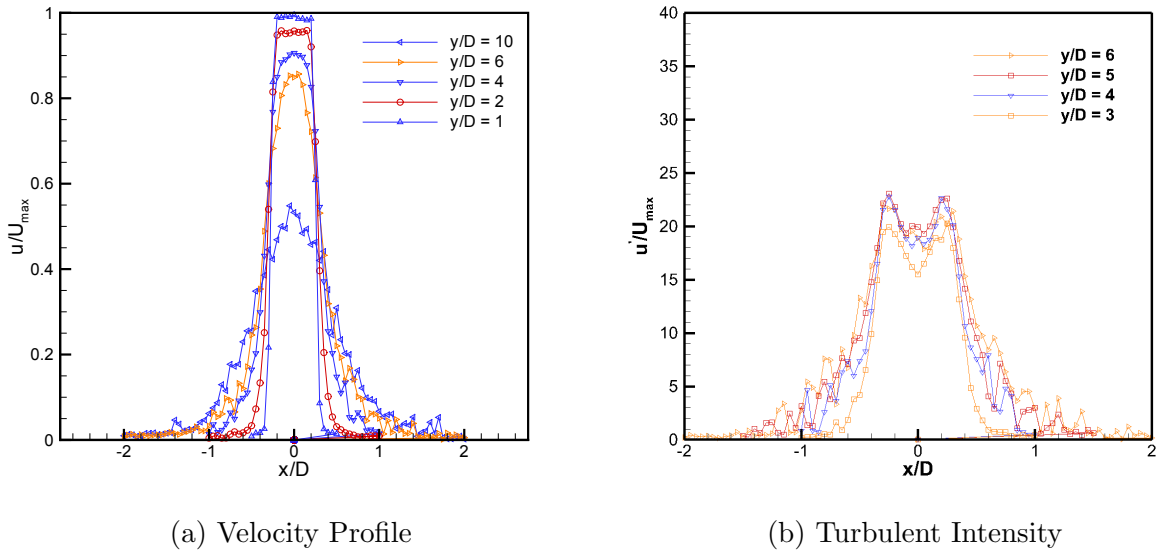
Figure 3.2: Unforced Jet

3.1 Baseline Jet

Velocity profiles were measured at several streamwise locations and are presented in Figure 3.2a. The potential core appeared to exist for approximately $2D$, the turbulent intensity at the nozzle exit is fairly low ($< \%3$). However, at $x/D > 3$ the turbulent intensity increased throughout the lateral direction of the jet. The shear layer displayed the highest levels of turbulence as expected.

Distribution of velocity for the unforced case was extracted from the PIV measurements and shown in Figure 3.3.

The momentum thickness and displacement thickness of the initial boundary layer were calculated from,

$$\delta_m \quad = \quad \int_0^{\frac{D}{2}} \left(\frac{u}{U_c} \right) \left(1 - \frac{u}{U_c} \right) dy \tag{3.2}$$

21
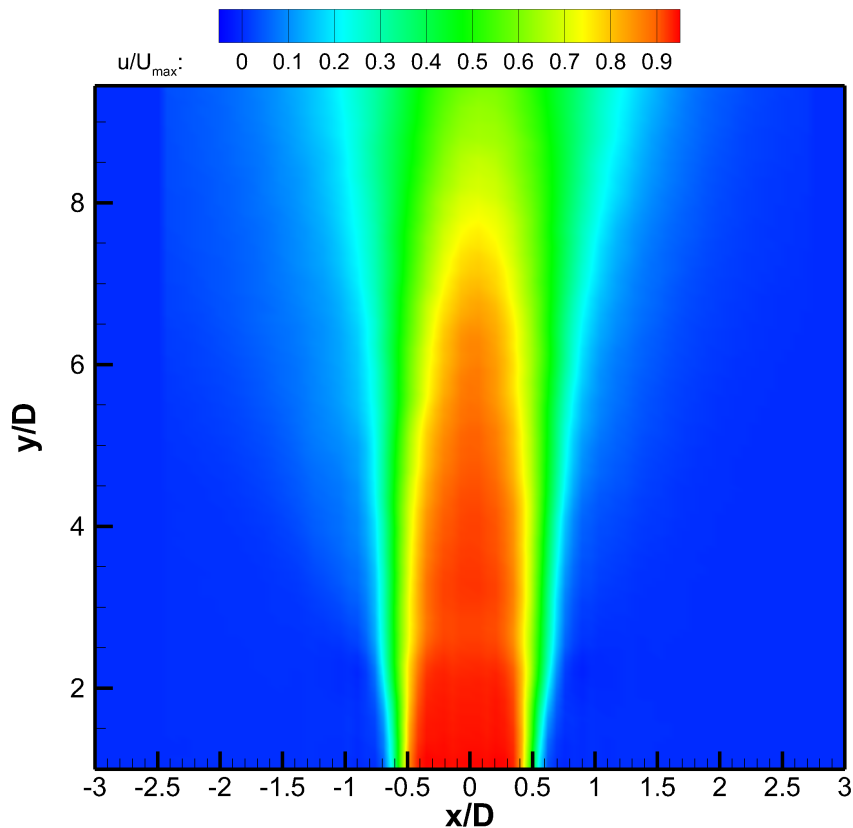
Figure 3.3: Velocity contour from PIV data, $Re = 5500$

$$\delta_d \quad = \quad \int_0^{\frac{D}{2}} \left(1 - \frac{u}{U_c}\right) dy \qquad (3.3)$$

respectively.

The values were calculated from the hot-wire traverse data at $y/D = 0.1$ are, $\delta_m = 0.0019$ and $\delta_d = 0.00860D$. These values found at the nozzle exit are congruent with the values found by Mi ($\delta_d = 0.004d, \delta_m = 0.0018d$ [23]) with the difference being attributed to Reynolds number.

Figure 3.4a shows the decay of centerline velocity for the unforced case up to $20D$. The data was fitted with a third degree polynomial. The curve is typical for round turbulent jets.

Figure 3.4b is the power spectral density of the round jet at the centerline of the nozzle exit at various y/D locations. The power spectrum was calculated using a Fourier transform of the velocity measurements made with the CTA. There is a clear dominant frequency located at the preferred instability ($150Hz$). As the probe was moved downstream to a more turbulent region the total energy increased.

3.2   Forcing

In the past both the preferred and sub-harmonic frequencies have been used. In the present work, an approximate harmonic of $50Hz$ was used for the forcing that resulted in a Strouhal number (St) of 0.12. The tests were also conducted and compared with a $St = 0.09$. The Strouhal number was calculated from,

$$St \quad = \quad \frac{fD}{U_{max}} \tag{3.4}$$

In addition to the frequency, the amplitude of the oscillation was also controlled through the DriveWare software. A peak-to-peak amplitude of 400 counts was set for $St = 0.12$ and 480 counts for $St = 0.09$. After taking into account losses in the transfer of energy from the arm to the iris and the tuning of the loops, the peak-to-peak amplitude was calculated to be $0.02D$.

3.2.1   Power Spectra

The power spectra of the forcing are displayed in Figure 3.5. At each downstream location, there is a visible peak at the forcing frequency. At $y/D = 1$ there is a sharp drop-off in amplitude after the forcing frequency. This is attributed to the forcing frequency attenuating the initial instabilities. However, as the distance downstream increased the drop-off decreased. Comparing the non-forcing to forcing conditions, it appeared that the

23
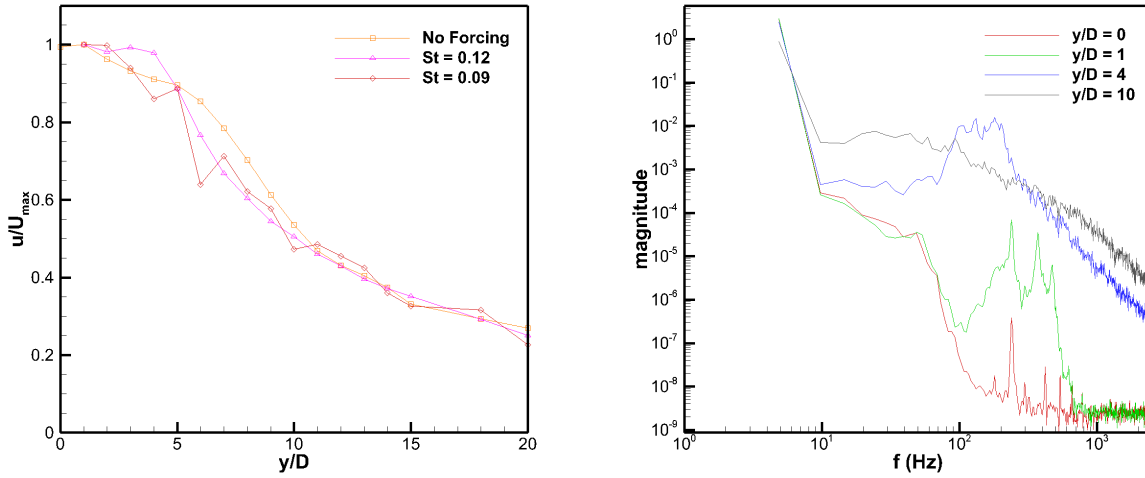
(a) Centerline Decay

(b) Velocity Spectra

Figure 3.4: Characteristics for unforced jet at $x/D = 0$

forcing introduced an instability earlier than expected. There are also a myriad of peaks from approximately $75 - 450Hz$. These double-peaks (f_a and f_b) appear to form at frequencies near the fundamental such that the average of f_a and f_b is the fundamental frequency and the range of f_a to f_b is the forcing frequency. Previous researchers have coined similar peaks "parametric resonance" which are typically induced by the fundamental and sub-harmonic frequencies [20]. However, in the current research the peaks appear attributed to harmonics of the forcing frequency.

Figure 3.6 shows turbulent intensity for the two forcing cases. It appears that the instability introduced by the forcing is making the jet more stable. This could be due to the introduction of a series of vortex rings near the exit plane.

Figure 3.7 compares the velocity profile from the hot-wire data. It is apparent in each image that the maximum velocity decay is only $5 - 10\%$ for the forcing cases as the location downstream approaches $20D$. Initial analysis hints that harmonic, low frequency excitation increases entrainment until approximately $10D$ downstream. It can conjectured that the excitation only attenuates the instabilities until $10D$.

(a) $St = 0.12$ (b) $St = 0.09$
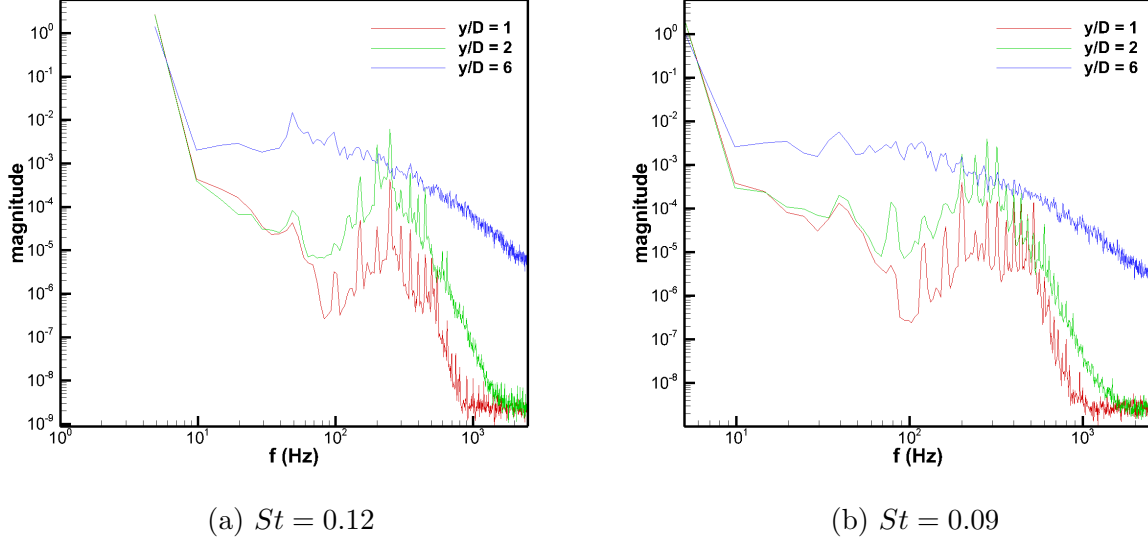
Figure 3.5: Velocity spectra, forced cases

Additional velocity contours of the forcing cases are located in Appendix C. Minimal information can be gathered by comparing the velocity contours of the forced cases to the unforced (Figure 3.3). Therefore a statistical method is incorporated to quantify the modifications and evolution of the energy distribution within the flow.

3.2.2 Proper Orthogonal Decomposition

The POD contour plots were created by reconstructing the velocity field with the eigenfunctions. The eigenfunctions are similar to the modes and represents a behaviour of the flow as mentioned in section 2.5.1. Each contour plot was then non-dimensionalized by the maximum value found from the non-forcing case to adequately compare different cases. The modal numbers were chosen because there was a change in the slope from the subsequent mode to the desired mode. The slope indicated an evolution in the energy. The modal distribution are located in Appendix E.

For the analysis on the streamwise cuts, the first and sixth eigenvalues are plotted. These eigenvalues were chosen because they are two of the principal modes for representing the dynamics of the large-scale structures and typically the first mode represents the "large

25
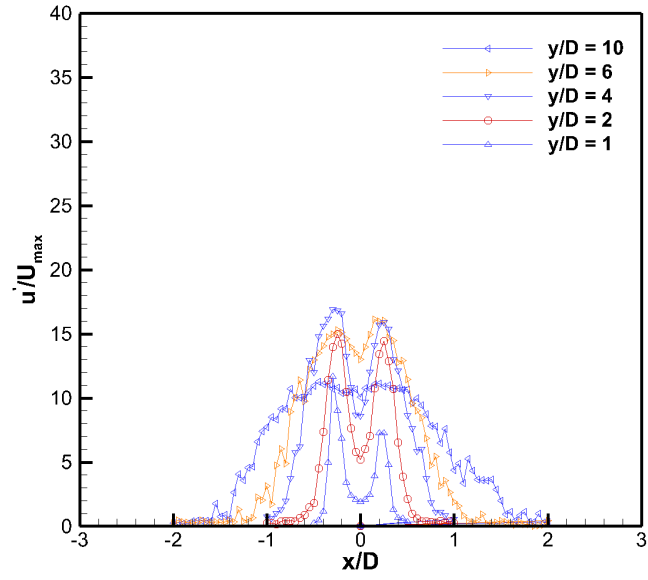
(a) $St = 0.12$
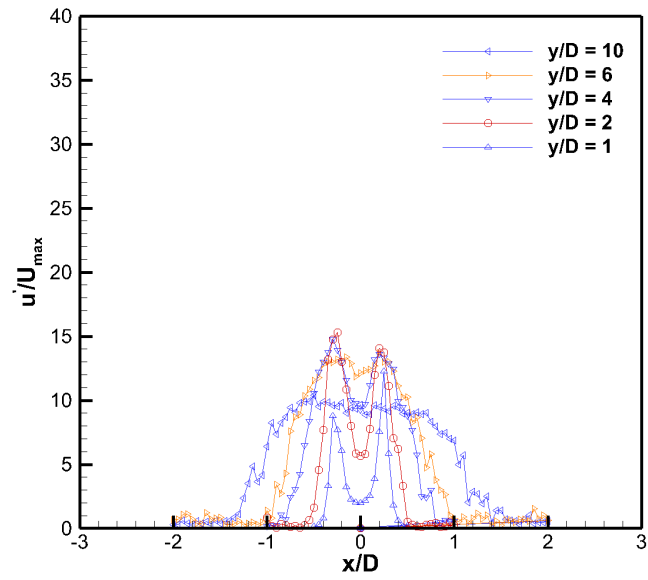
(b) $St = 0.09$

Figure 3.6: Turbulent Intensity, forced cases
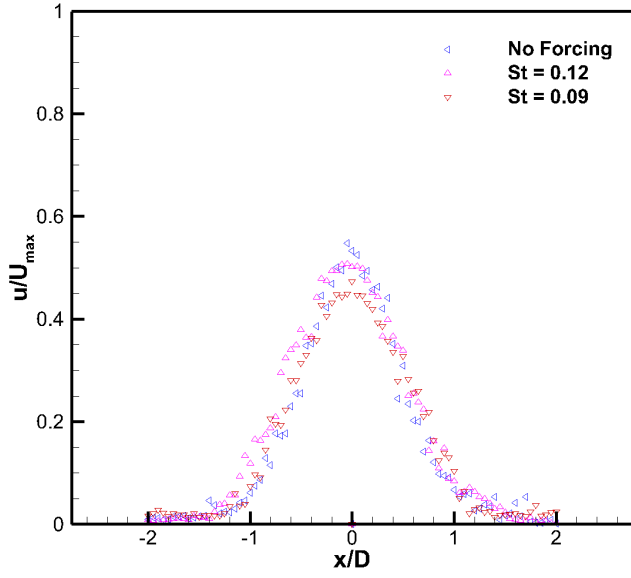
(a) $y/D = 10$
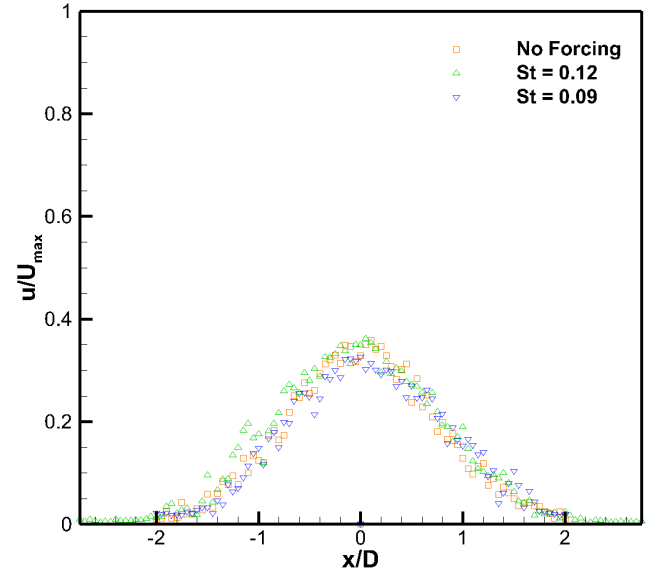
(b) $y/D = 15$
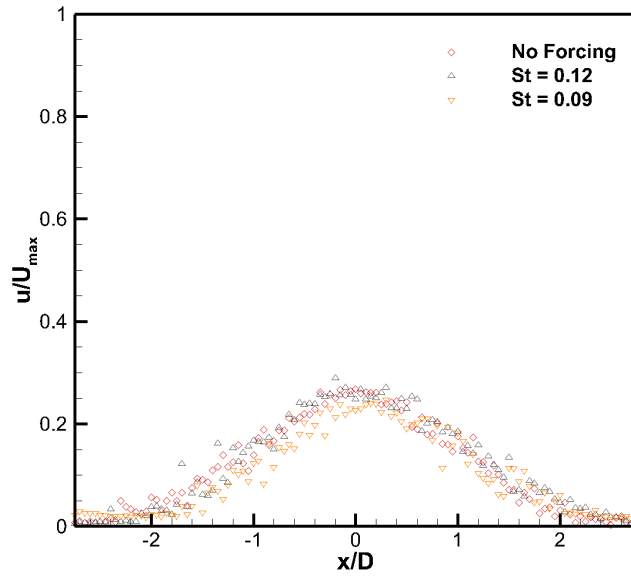
(c) $y/D = 20$

Figure 3.7: Comparison of velocity profiles for the forced an unforced cases
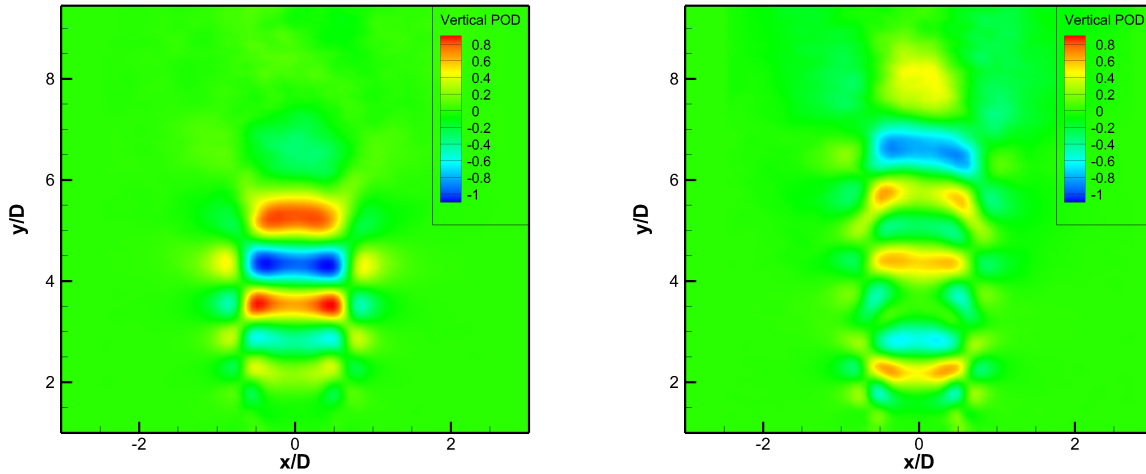
(a) First mode

(b) Sixth mode

Figure 3.8: Mode energy, unforced case

eddies" in the flow [14]. In Figure 3.8a the large scale vortex rings are clearly visible with alternating positive and negative fluid advection patterns. They appear to first become visible at approximately $2D$ and exist up to $6D$. The absence of clean indication of vortex rings after $6D$ is attributed to the coalescesing of rings similar to Figure 1.2 which leads to the formation of unstable vortices. The unsteadiness of vortex pairing increases the likelihood of vortex breakdown

Figure 3.8b represents the energy content of the sixth mode. Two distinct structures are visible in this mode. The structures with positive velocity-direction appear to be located on the zenith of the individual vortex rings and maintain symmetry about the axis of the jet and are likely due to the streamwise vortex filaments wrapping around the large-scale structure. As the vortex filaments stretch, the axial strain results in an increase in vorticity that in turn increases the entrainment.

The asymmetric structure with a negative velocity direction in Figure 3.8b is similar in geometry and strength to the large-scale structures seen in the previous image, however the energy content is substantially less. The structure is most similar to the structure at $y/D \approx 2.75$ in Figure 3.8a.
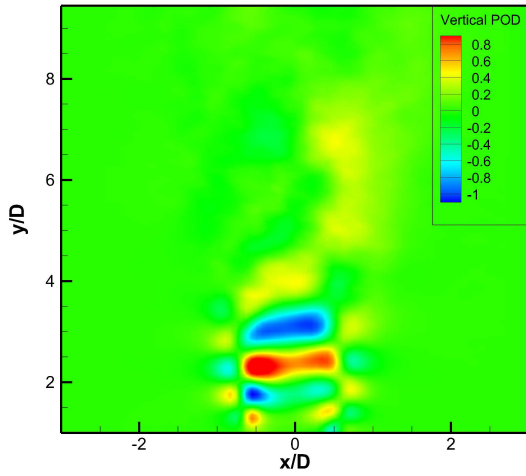
(a) First mode, $St = 0.12$
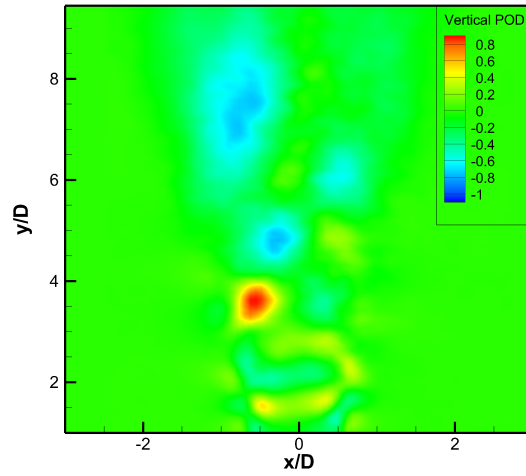
(b) Sixth mode, $St = 0.12$
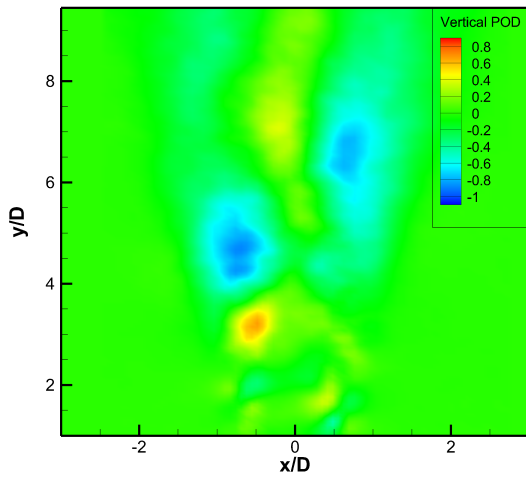
(c) First mode, $St = 0.09$
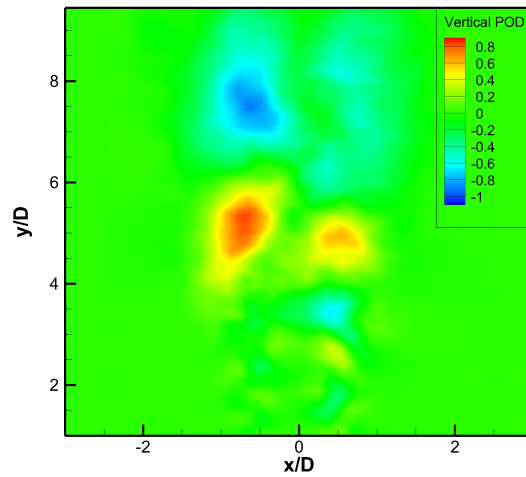
(d) Sixth mode, $St = 0.09$

Figure 3.9: POD modes - forced jet

With the loss of symmetry on the right hand side of the structure and similar velocity to the aforementioned structure it is conjectured that the modal content at $y/D \approx 6.75$ in Figure 3.8b depicts the decay of vortex rings into smaller structures. This would be due to the "leap frog" effect or vortex roll-up of subsequent vortices which in turn increase the susceptibility of vortex breakdown.

Azimuthal contour plots of the flow were also taken at this vertical location to analyze the modal distribution and to gain insight into these instabilities (Figure 3.10) at $y/D = 4$. The results are presented in Figures 3.10, 3.12, and 3.14. Vectors were superimposed on the image, to add clarity on the direction of the flow within the specific mode. To extrapolate the flow in the y-direction continuity must be used, i.e., if the x and z radial components are small the y velocity component must be large.

In Figure 3.10a, the regions of high contrast are evident of symmetric large-scale structures. Figure 3.10b represents the 25th POD mode, this mode was chosen because it corresponded to the highest mode calculated and these modes can be related to the finer scale of turbulence. Even though this mode contains the smallest percentage of energy at the azimuthal location it is ample relative to other locations and the non-forcing case. This is confirmed by interpolating the lines in Figure 3.5. In Figure 3.10b, there appear to be two counter rotating streamwise filaments or "braids" within this mode from the vectors. The centroids of the braids are approximately at: $(0.25, \ 0.3), \ (-0.35, -0.4), \text{and} \ (0.05, -0.1)$. This is in contrast to the contour plot which indicates four pairs of vertical flow. This is possibly due to the top-half of the image, which appears to be dependent on two saddle points. A saddle point is a type of critical point that commonly represents a two-dimensional surface where one direction curves up and the other curves down. The surface curvature more closely represents a line than parabolic curve but still indicates a two-dimensional structure within the 25th mode. There appears to be two saddle points symmetric about the x-axis at $x/D = \pm 0.5$. The flow travels at approximately an $\pm 45 \deg$ angle with respect to negative z. The flow then bifurcates at the critical point and either travels towards the center or away from the centerline.

For $St = 0.12$ and 0.09 (Figure 3.12a and 3.13a) there are similarities in the energy content of the first mode. Both images shown lack of large-scale structures and parallel, non-obstructed flow.
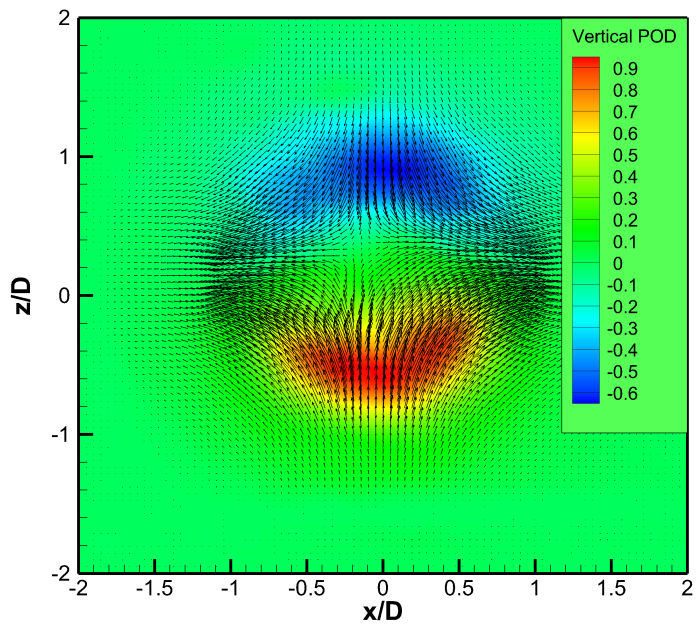
(a) Mode 1
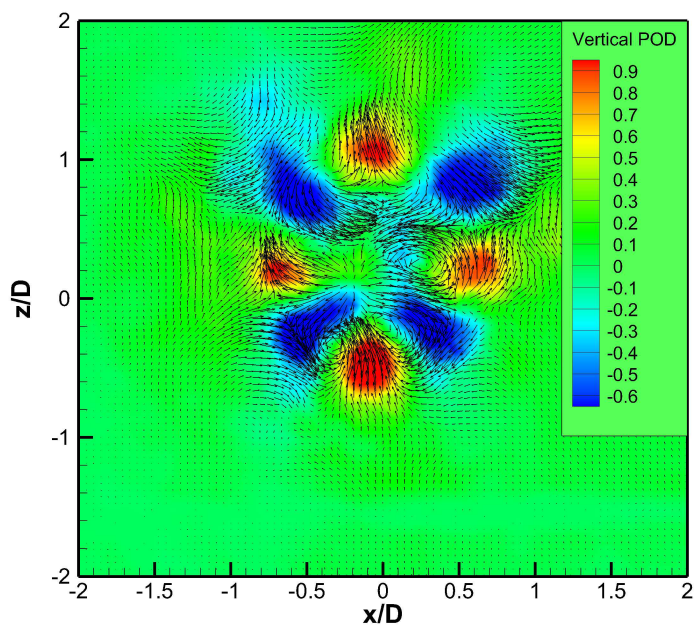
(b) Mode 25

Figure 3.10: POD of transverse plane at $y/D = 4$

The harmonic forcing frequency ($St = 0.12$) attenuated large-scale structures at $y/D = 4$ and it appears from Figure 3.9a that the forcing introduced low frequency instabilities at this location. These instabilities can be in the form of large-scale structures but it is not conclusive from the POD. For sub-harmonic ($St = 0.09$) the forcing attenuated the low frequency instabilities at all vertical locations, not only the specific location.

In the 25th POD mode the sub-harmonic forcing appears to skew the radial advection pattern. In Figure 3.12b, the streamwise vortices have meandered through the flow and appear to form an isosceles triangle. This could be due to the filaments beginning to diffuse and weakening or an imposed oscillation of the filaments due to the forcing. The ability of the streamwise filaments to entrain fluid is evident on the right-hand-side of the contour. The center of one of the vortices is approximately at, $(0.4, -0.1)$. This filament ejects and then quickly entrains the ejected fluid as well as surrounding fluid. This shows that the streamwise vortices do increase the entrainment of ambient fluid.

For $St = 0.09$ (Figure 3.13b) only one streamwise filament but is weaker than in the previous forcing condition. This mode also appears to be dominated by nodal critical points. This is depicted by the fluid travelling away from the node. Higher levels of turbulence were noted in this mode.

In addition to the time average snapshots (Figure 3.10, 3.12, and 3.14), instantaneous images were examined that showed the vortex breakdown and asymmetry as the distance downstream increased and is shown in Figure 3.11. At $y/D = 4$, there is a saddle that spans approximately $225°$, it is also outlined in red. This was determined due to the expected flow direction at the azimuth of the structure. The effect that large-scale structures have on entrainment is also depicted by the streamtracers. The flow outside of the jet is directed to the origin and being pulled underneath the "mushroom" shape of the structures into the core. The black arrows in the center image depict the location of the entrainment.

There is also an asymmetric vortex breakdown partially due to visible streamwise counter rotating vortex filaments indicated by large black arrows. Coalescing of vortex
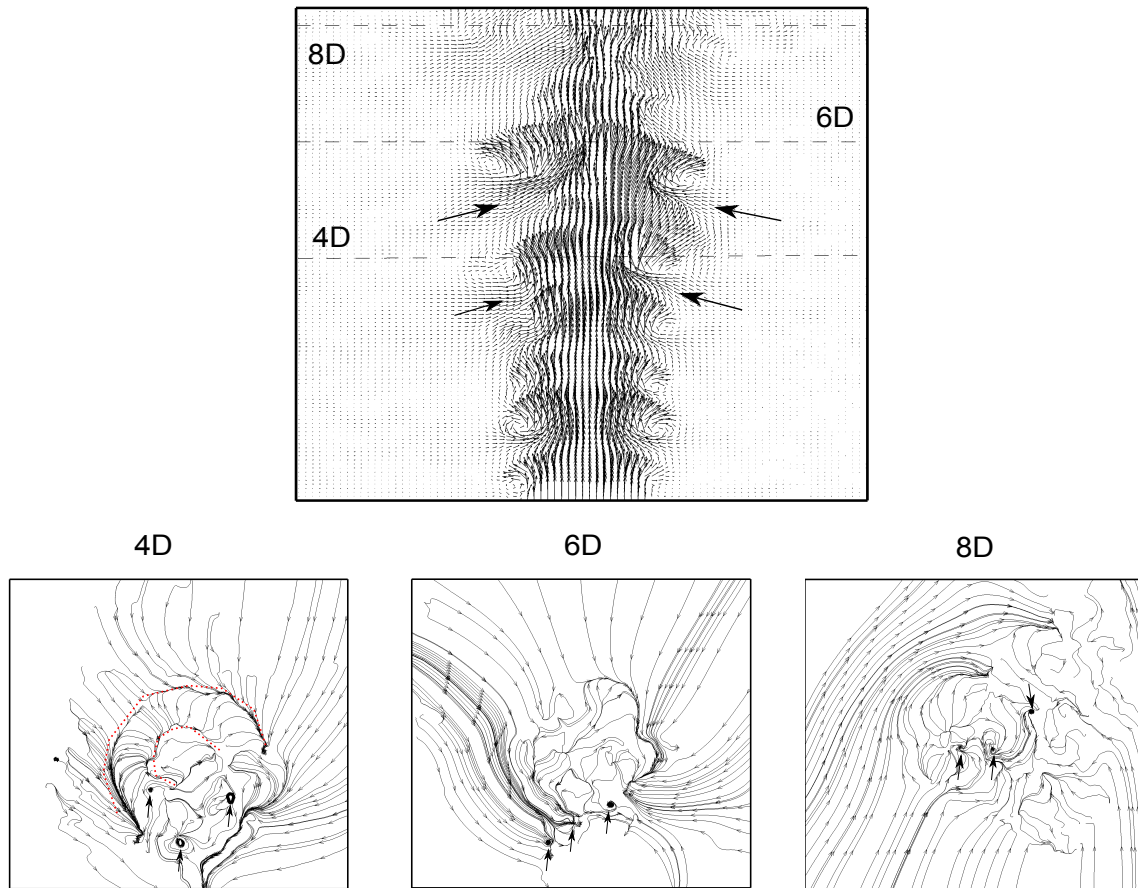
Figure 3.11: PIV single image with azimuthal cuts at $y/D = 4D, 6D$, and $8D$

rings also makes them more susceptible to vortex breakdown due to decreasing the strength and convection. This, however, was not be visualized in the azimuthal instantaneous images. These vortical structures are important in the entrainment process, they advect the quiescent fluid into the jet flow.

As the distance downstream increases, the vortex breakdown engulfs nearly the entire structures. The streamwise vortices meander within the flow indicating either a swirling motion of the jet or a natural oscillating motion of the vortices.

Figure 3.9 shows the effect of azimuthally forcing of the jet at the desired Strouhal number. For the first case ($St = 0.12$) the forcing energizes the initial instability and hastens

the growth of the instability into large scale structures. There is also a loss of symmetry within the apparent vortex rings. From these images it is difficult to conclude whether the asymmetry is due to the forcing mechanism or addition of a asymmetry mode. McIlwain and Pollard used an LES to investigate the near field of round jets. They noted a vortex ring located at $x/D \approx 2$ and despite the perfectly symmetry forcing the ring was slightly distorted which they attributed to the presence of a negative helical mode, $m = -1$ [40].

In the sixth POD mode there is complete loss of symmetry or organized structures near the nozzle exit plane. What is left are aperiodic markers or turbulence. In Figure 3.9c it is evident that forcing at a frequency other than the harmonic attenuates the formation of any large scale structures. In jets, fluid entrainment is mainly due to large scale structures and vortex pairing and since the structures are attenuated at the exit, entrainment and velocity decay should be minimal. According to Figure 3.7a, the centerline decay and fluid entrainment as a function of the velocity profile are similar for the non-forcing, $St = 0.12$ and $St = 0.09$ conditions. A possibility, is that the streamwise vortices increase the entrainment of ambient fluid. This can occur due to the high strain field formed by the vortices, increases the velocity in the azimuthal direction.

3.2.3 Symmetry Analysis

Two probes were placed in the shear layer $(0.75D, \ 2D)$ to give additional insight into the asymmetry of the jet (Figure 3.15). Figure E.2 show the streamwise velocity fluctuations, $u_1^{'}$ and $u_2^{'}$. There is evidence of a asymmetry in the non-forcing condition that was otherwise undistinguished. This is evident from the slight phase shift at various time intervals. However, from $t = 20 \ ms$ to approximately $37 \ ms$ there is commonality within the fluctuations indicated a varicose or symmetric mode.

Both forcing cases increase the asymmetry of the instabilities. The forcing also introduces a large velocity increase. These outlying fluctuations have multiple peaks which could indicate that there are multiple instabilities attributing to the rapid increase. In Figure 3.16c

34

there are a myriad of peaks at the base of the outlying fluctuation. This can be indicative of the parametric resonance originally seen in the PSD plots of Figure 3.5.

Cross-spectra analysis was also conducted on the signals. The spectra is located in Appendix D. In Figure 3.16a the average of the curve is zero, indicating that the magnitudes of the structures measured by the two probes are similar. In Figures D.2 and D.3 there is a non-zero average indicating a variation in the structure magnitude. It can also be extrapolated that the variation of structure magnitude would indicate an asymmetry or helical mode.

3.2.4 Reynolds Shear Stress

Reynolds shear stresses (τ_{xy}) were calculated from,

$$\tau_{xy} = \frac{\varrho \overline{u'v'}}{U_{max}^2} \tag{3.5}$$

where the overbar corresponds to the averaged quantity.

Reynolds shear stress are in Figures 3.17 and 3.18. In the no forcing case, there is a small region near the nozzle exit plane due to the shear and growth of the initial instability. After that, τ_{xy} is not visible until $y/D \approx 4$, and then there is a lateral and streamwise growth.

For the forcing cases, τ_{xy} is visible and grows near the nozzle exit plane. This is due to the earlier formation and growth of the large scale structures seen in Figure 3.9a. In Figure 3.18a the color contour plot has a higher level than both the non-forcing and forcing at $St = 0.09$. This is due to the combination of the forcing mechanism adding energy into the flow and the formation of large scale structures closer to the nozzle exit plane. It would be expected to see the same results at $St = 0.09$, except the sub-harmonic attenuated all large scale structures.

3.2.5 Turbulent Kinetic Energy

The turbulent kinetic energy (TKE) was calculated from the following equation,

$$TKE = \frac{\overline{u'^2} + \overline{v'^2}}{2U_{max}^2} \tag{3.6}$$

The largest region of kinetic energy is located in the center of the shear layer for the non forcing condition (Figure 3.19). This is due to the predominately large fluctuations in the u component from the rotation of the large scale structures. For the forcing conditions (Figure 3.20a and 3.20b) the maximum TKE is substantially less. This is attributed to the forcing that quickly attenuated the large scale structures. For $St = 0.12$, there is a small region of higher TKE than for $St = 0.09$ and this is because of the low frequency energy that was introduced by the forcing and evident in Figure 3.9a.

Appendix H contains the same figures but with contour lines superimposed to distinguish regions of similar color.
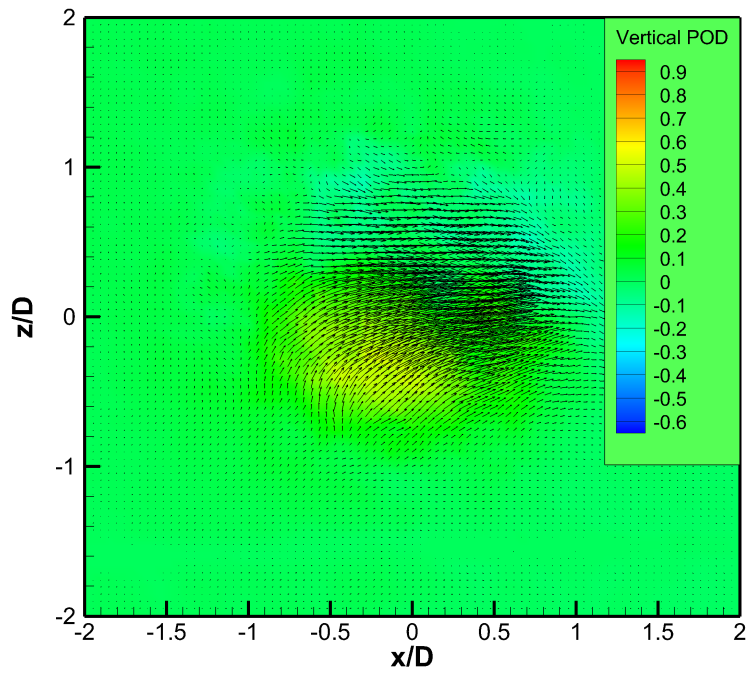
(a) First mode, $St = 0.12$
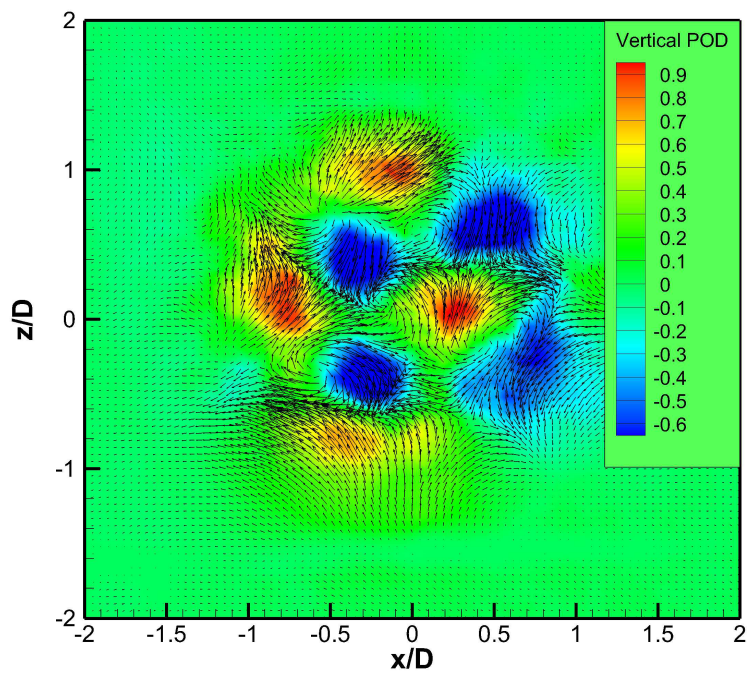
(b) 25th mode, $St = 0.12$

Figure 3.12: POD of transverse plane at $y/D = 4$ ($St = 0.12$)
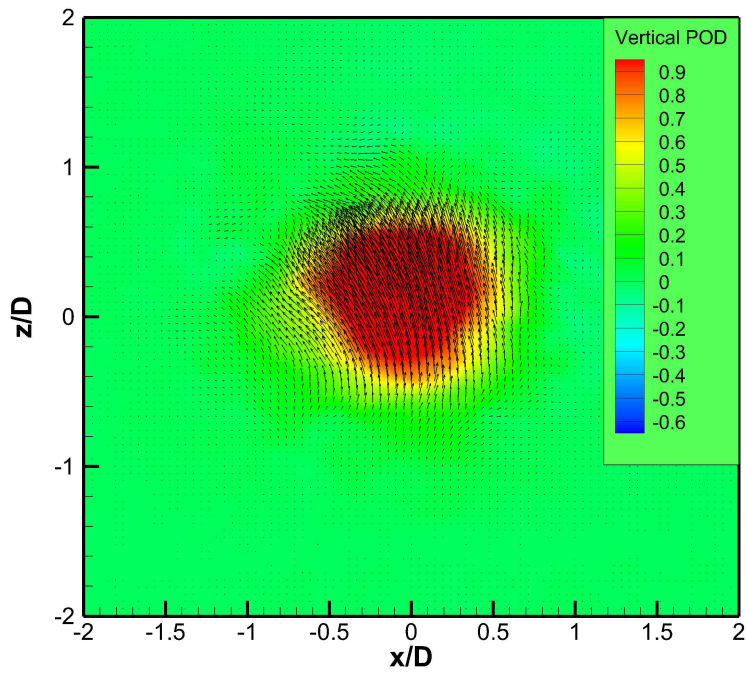
(a) First mode, $St = 0.09$
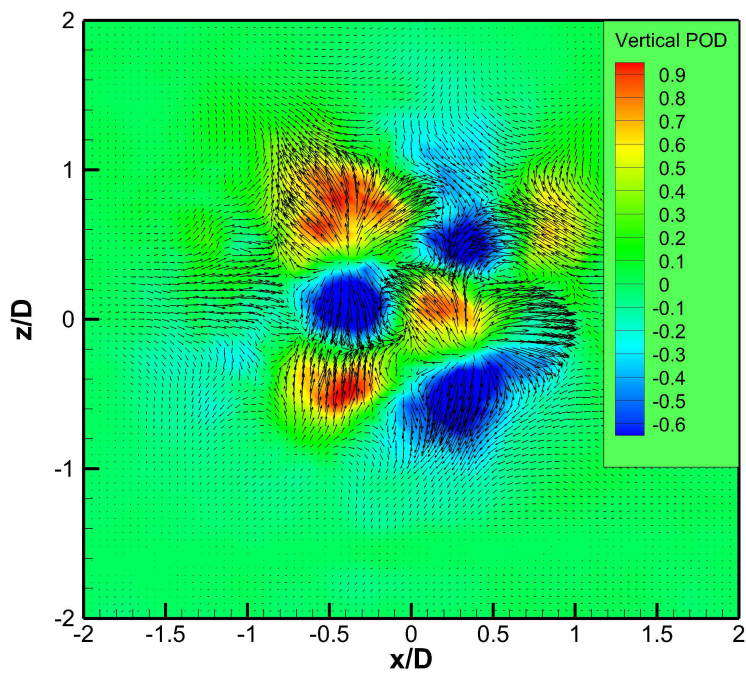
(b) 25th mode, $St = 0.09$

Figure 3.13: POD of transverse plane at $y/D = 4$ ($St = 0.09$)
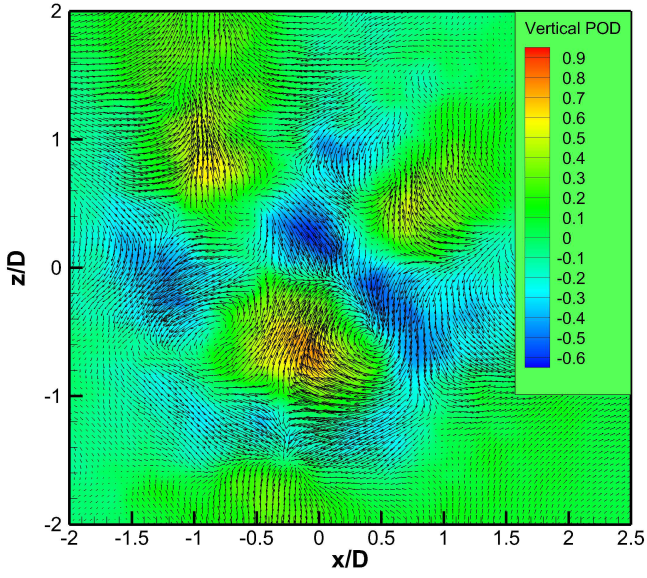
(a) No forcing
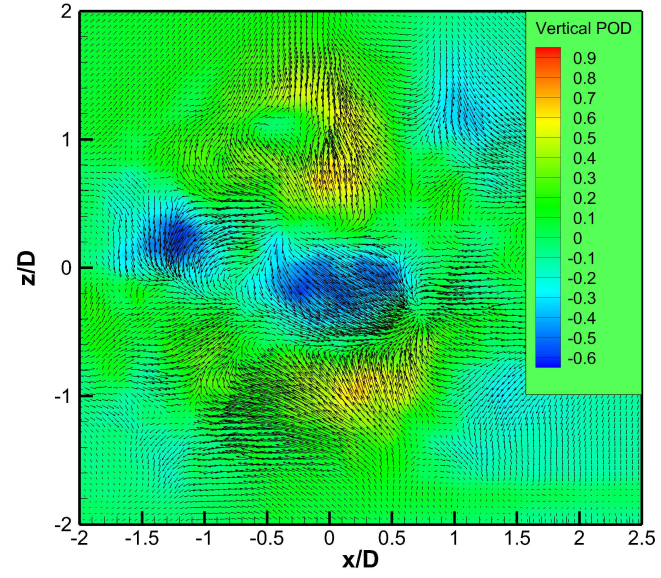
(b) $St = 0.12$
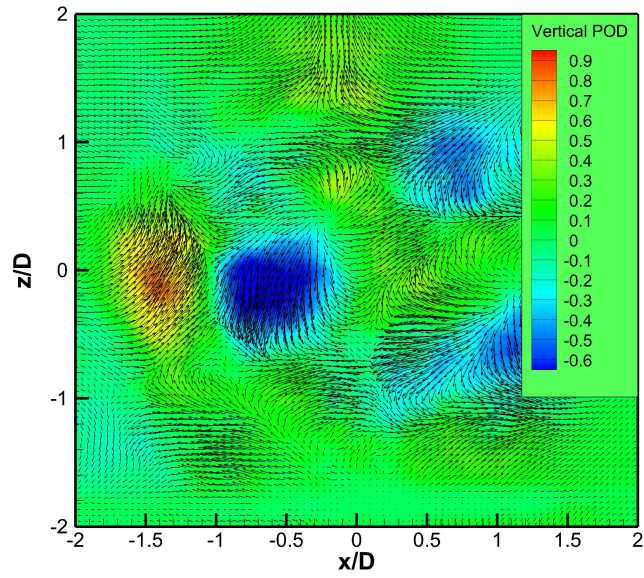
(c) $St = 0.09$

Figure 3.14: 25th POD mode at $y/D = 6$
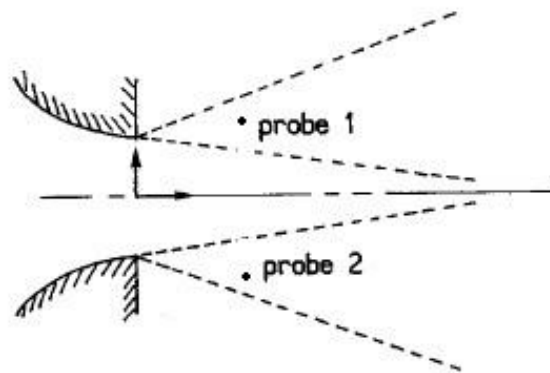
Figure 3.15: Location of two probes
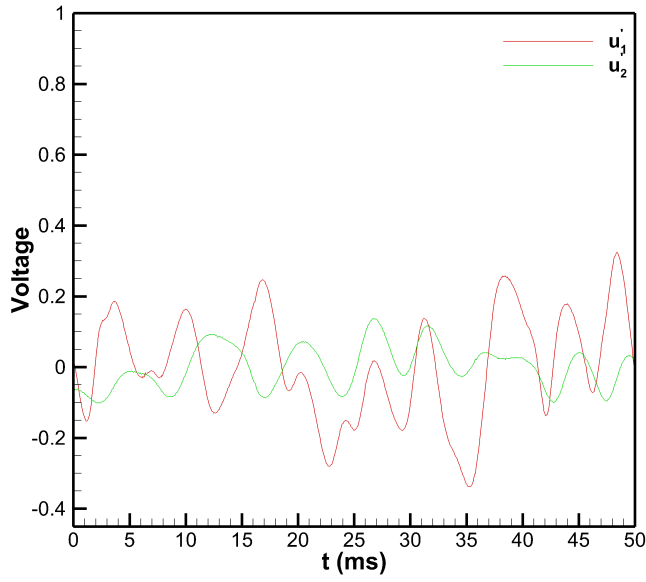
(a) No forcing
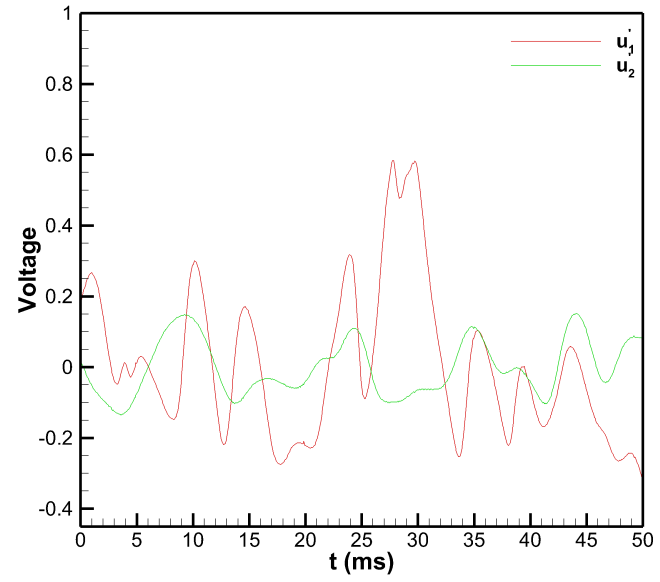
(b) $St = 0.12$
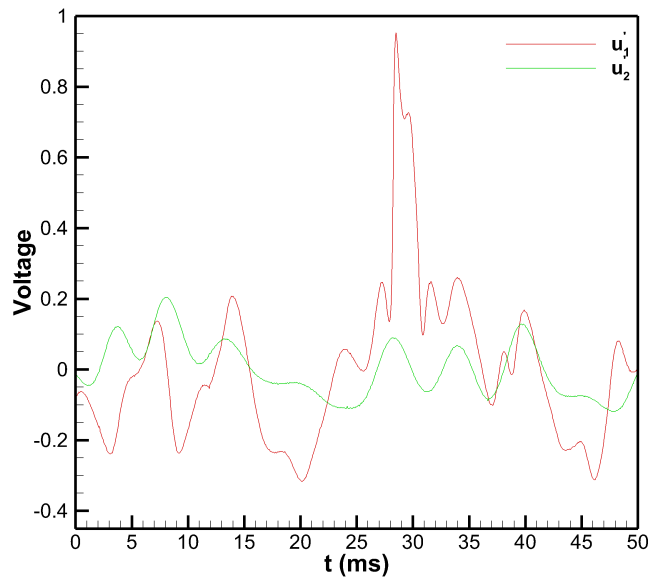
(c) $St = 0.09$

Figure 3.16: Flow structure behaviour, probes are located at $(\pm 0.75D, 2D)$
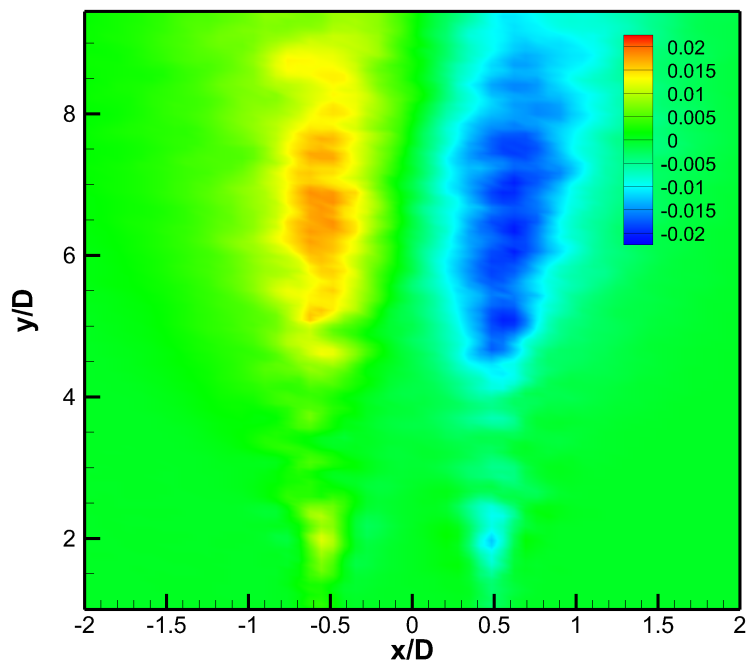
Figure 3.17: Reynolds shear stress (τ_{xy})
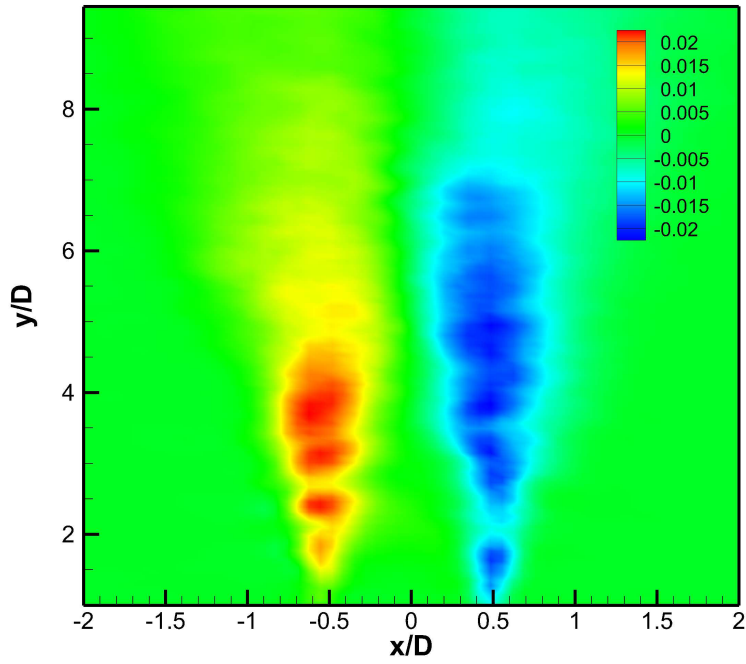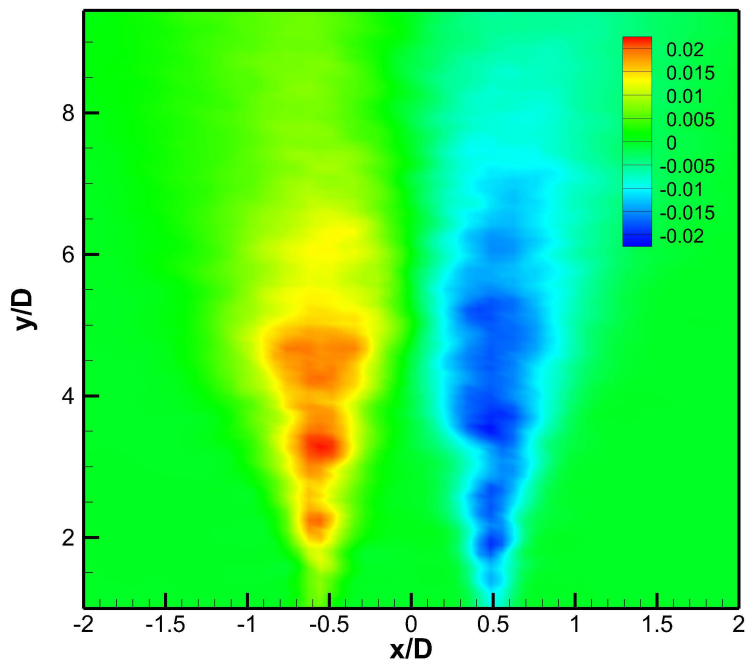
(a) $St = 0.12$

(b) $St = 0.09$

Figure 3.18: Reynolds shear stress for forced cases
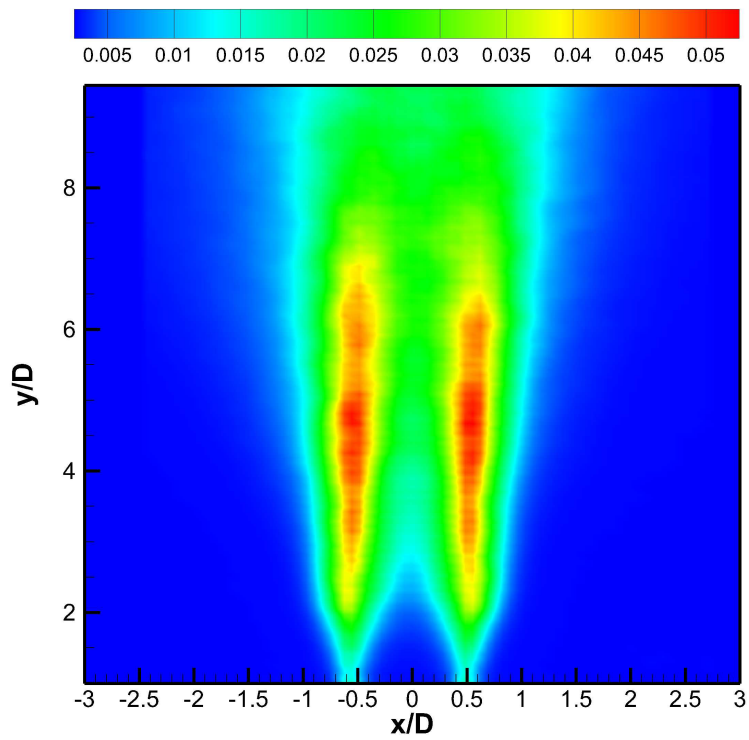
Figure 3.19: Turbulent Kinetic Energy for non-forcing
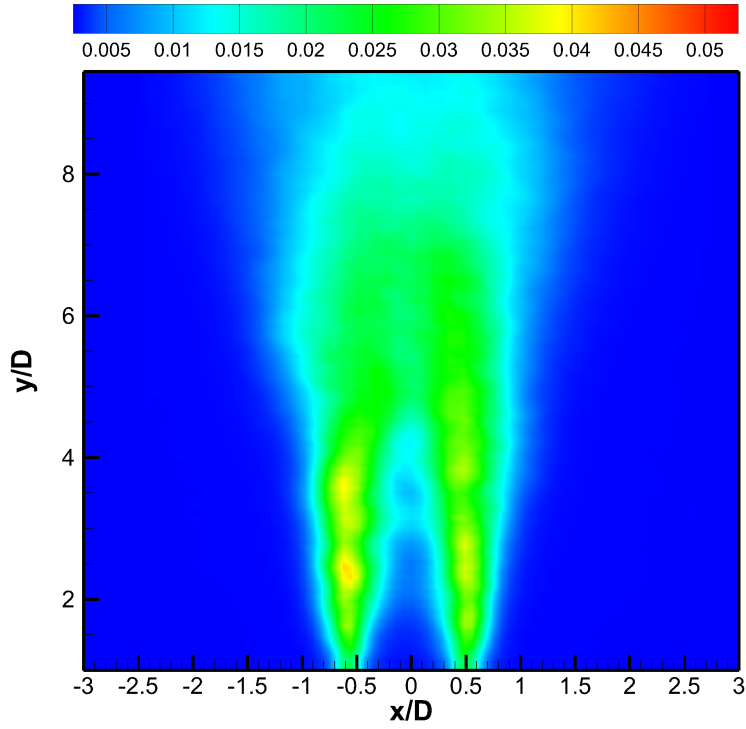
(a) $St = 0.12$
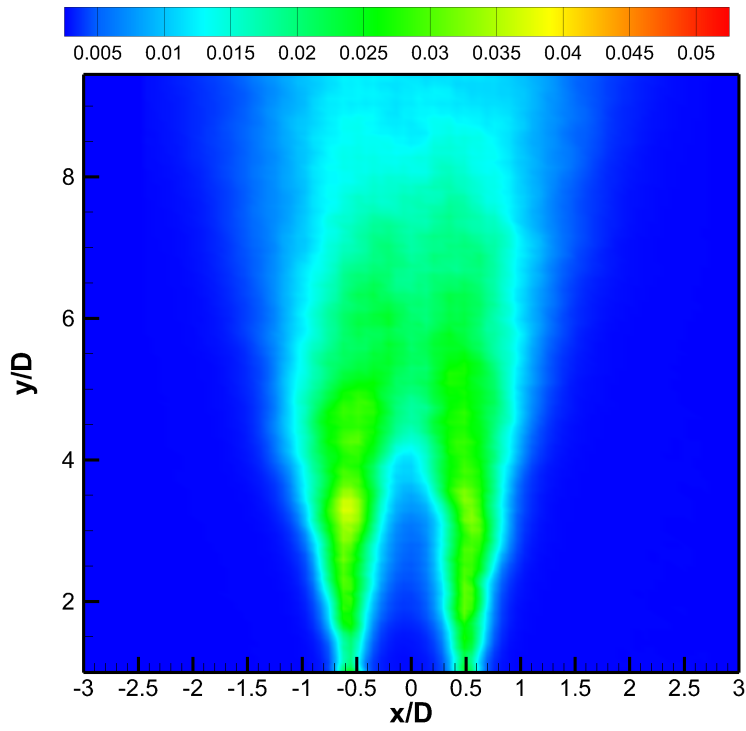
(b) $St = 0.09$

Figure 3.20: Turbulent Kinetic Energy for forced cases

45

Chapter 4

Conclusions

A round axisymmetric turbulent jet was subjected to azimuthal excitation at various forcing frequencies. A forcing mechanism was used to azimuthally excite the flow in $360°$. The experiments were conducted at Reynolds number of $5,500$ and forcing frequencies with equivalent Strouhal numbers of 0.12 and 0.09. Both forcing frequencies resulted in an increase in the entrainment from the streamwise vortex filaments and increase the asymmetry of the large scale structures.

The harmonic frequency, $St = 0.12$, attenuated the large scale structures as evident in the PIV and POD analysis. The instabilities appeared to be in the form of large scale vortex rings. The forcing case also appeared to introduce low frequency instabilities near the nozzle exit plane ($y/D = 2$). There was also a higher level of τ_{xy} not only within the first four diameters downstream but also throughout the flow and a slightly higher TKE near the exit plane due to the velocity fluctuations of the low frequency inabilities introduced by the forcing.

For $St = 0.09$, all large scale structures were attenuated and unlike the harmonic frequency, low frequency instabilities were not introduced into the flow. This forcing frequency also increased the sinuous instability as evident from the u' comparisons.

Bibliography

[1] Yule, A., "Investigation of Eddy Coherence in Jet Flows," *The Role of Coherent Structures in Modelling Turbulence and Mixing*, edited by J. Jimenez, Vol. 136, Springer-Verlag, 1980, pp. 188–207.

[2] TSI, *IFA 300 Constant Temperature Anemometer System*, revision d ed., December 2010.

[3] Mi, J., Nathan, G., and Luxton, R., "Mixing Characteristics of a Flapping Jet from a Self-Exiciting Nozzle," *Flow, Turbulence, and Combustion*, Vol. 67, 2001, pp. 1–23.

[4] Ritchie, B., Mujumdar, D., and Seitzman, J., "Mixing in Coaxial Jets Using Synthetic Jet Actuators," *American Institute of Aeronautics and Astronautics*, 2000.

[5] Brown, G., "On Sensitive Flames," *Philosophical Magazine*, Vol. 13, No. 82, 1932.

[6] Panton, R. L., *Incompressible Flow*, New York: J. Wiley, 1996, 2nd ed.

[7] Crow, S. and Champagne, F., "Orderly Structure in Jet Turbulence," *Journal of Fluid Mechanics*, Vol. 48, No. 03, August 1971, pp. 547–591.

[8] Yule, A., "Large-Scale Structure in the Mixing Layer of a Round Jet," *Journal of Fluid Mechanics*, Vol. 89, No. 3, 1978, pp. 413–432.

[9] Fiedler, H., "Coherent Structures in Turbulent Flows," *Progress in Aerospace Sciences*, Vol. 25, No. 3, 1988, pp. 231–269.

[10] Lau, J., Fisher, M., and Fuchs, H., "The Intrinsic Structure of Turbulent Jets," *Journal of Sound and Vibration*, Vol. 22, No. 4, 1972, pp. 379.

[11] A.S. Ginevsky, Y.V. Vlasov, e. a., "Acoustic Control of Turbulent Jets," *Foundations of Engineering mechanics*.

[12] Becker, H. and Massaro, T., "Vortex Evolution in a Round Jet," *Journal of Fluid Mechanics*, Vol. 31, No. 3, 1968, pp. 435–558.

[13] Dimotakis, P. E., MiakeLye, R. C., and Papantoniou, D. A., "Structure and Dynamics of Round Turbulent Jets," *Physics of Fluids*, Vol. 26, No. 11, November 1983, pp. 3185–3192.

[14] Citriniti, J. and George, W., "Reconstruction of the Global Velocity Field in the Axisymmetric Mixing Layer Utilizing the Proper Orthogonal Decomposition," *Journal of Fluid Mechanics*, Vol. 418, 2000, pp. 137–166.

[15] Patte-Rouland, B., Lalizel, G., Moreau, J., and Rouland, E., "Flow Analysis of an Annular Jet by Particle Image Velocimetry and Proper Orthogonal Decomposition," *Measurement Science and Technology*, Vol. 12, 2001, pp. 1404–1412.

[16] Gordeyev, S. and Thomas, F., "Coherent Structure in the Turbulent Planar Jet. Part 1. Extraction of Proper Orthogonal Decomposition Eigenmodes and Their Self-Similarity," *Journal of Fluid Mechanics*, Vol. 414, 2000, pp. 145–194.

[17] Bernero, S. and Fiedler, H., "Application of Particle Image Velocimetry and Proper Orthogonal Decomposition to the Study of a Jet in a Counterflow," *Experiments in Fluids*, 2000, pp. S274–S281.

[18] Semeraro, O. and Bellani, G., "Analysis of Time-Resolved PIV Measurements of a Confined Turbulent Jet using POD and Koopman Modes," Vol. 53, 2012, pp. 1203–1220.

[19] Wickersham, P., *Jet Mixing Enhancement By High Amplitude Pulse-FLuidic Actuation*, Ph.D. thesis, Georgia Institute of Technology, 2007.

[20] Huang, J.-M. and Hsiao, F.-B., "On the Mode Development in the Developing Region of a Plane Jet," *Physics of Fluids*, Vol. 11, No. 7, July 1999, pp. 1847–1857.

[21] Deo, R. C., *Experimental Investigation of th Influence of Reynolds Number and Boundary Conditions on a Plane Air Jet*, Ph.D. thesis, The University of Adelaide, 2005.

[22] Reynolds, W., Parekh, D., and Juvet, P., "Bifurcating and Blooming Jets," *Annual Review of Fluid Mechanics*, Vol. 35, January 2003, pp. 295–315.

[23] MI, J., Nobes, S., and Nathan, G., "Influence of Jet Exit Conditions on the Passive Scalar Field of an Axisymmetric Free Jet," *Journal of Fluid Mechanics*, Vol. 432, 2001, pp. 91–125.

[24] Richards, C. and Pitts, W., "Global Density Effects on the Self-Preservation Behaviour of Turbulent Free Jets," *Journal of Fluid Mechanics*, Vol. 254, 1993, pp. 417–435.

[25] Dowling, D. R. and Dimotakis, P. E., "Similarity of the Concentration Field of Gas-Phase Turbulent Jets," *Journal of Fluid Mechanics*, Vol. 218, 1990, pp. 109–141.

[26] George, W. K., "The Self-Preservation of Turbulent Flows and Its Relation to Initial Conditions and Coherent Structures," *Advances in Turbulence*, Hemisphere, 1989, pp. 39–73.

[27] Dimotakis, P. E., "Some Issues on Turbulent Mixing and Turbulence," GALCIT Report FM93-1, March 1993, Updated as FM93-1a.

[28] Samimy, M., Reeder, M. F., and Zaman, K. B. M. Q., "Effect of tabs on the flow and noise field of an axisymmetric jet," *AIAA Journal*, Vol. 31, April 1993, pp. 609–619.

[29] Aydemir, E., Worth, N., and Dawson, J., "The Formation of Vortex Rings in a Strongly Forced Round Jet," *Experimental Fluids*, Vol. 52, 2012, pp. 729–742.

[30] Sirohi, J. and Chopra, I., "Fundamental Understanding of Piezoelectric Strain Sensors," *Journal of Intelligent Material Systems and Structures*, 2000.

[31] "Guide to Modern Piezoelectric Ceramics," Morgan Matroc Inc, March 1993.

[32] Koso, T. and Kinoshita, T., "Agitated Turbulent Flowfield of a Circular Jet with an Annular Synthetic Jet Actuator," *Journal of Fluid Science and Technology*, Vol. 27, No. 2, 2008, pp. 323–333.

[33] Pothos, S. and Longmire, E. K., "Asymmetric Forcing of a Turbulent Rectangular Jet with a Piezoelectric Actuator," *Physics of Fluids*, Vol. 13, No. 5, 2001, pp. 1480–1492.

[34] Wiltse, J. M. and Glezer, A., "Direct Excitation of Small-Scale Motions in Free Shear Flows," *Physics of Fluids*, Vol. 10, No. 8, 1998, pp. 2026–2037.

[35] Parker, R., Rajagopalan, S., and Antonia, R., "Control of an axisymmetric jet using a passive ring," *Experimental Thermal and Fluid Science*, Vol. 27, 2003, pp. 545–552.

[36] Chopra, M., "Hot Wire Anemometry and Fluid Flow Measurement," University Lecture, 2008.

[37] Jergensen, F. E., *How to Measure Turbulence with Hot-Wire Anemometers*, Dantec Dynamics, 2002.

[38] Perry, A. E., *Hot-Wire Anemometry*, Clarendon Press, 1982.

[39] Lumley, J. L., "The Structure of Inhomogeneous Turbulent Flows," *Atmospheric turbulence and radio propagation*, edited by A. M. Yaglom and V. I. Tatarski, Nauka, Moscow, 1967, pp. 166–178.

[40] Mcllwain, S. and Pollard, A., "Large Eddy Simulation of the Effects of Mild Swirl on the Near Field of a Round Free Jet," *Physics of Fluids*, 2002.

[41] Raffel, M., Willert, C. E., and Kompenhans, J., *Particle Image Velocimetry: a Practical Guide*, Springer-Verlag, 1998.

Appendices

Appendix A

Uncertainty Analysis

A statistical analysis was conducted to ensure the accuracy of the hot wire data collected according to the method described by Dantec Dynamics ([37]). The Re of 5,500 corresponding to 7.2 m/s was chosen. The sources of uncertainty that were considered are as follows.

1. Pressure transducer error

   From the manufacturer specifications, the accuracy of the transducer was found to be 0.5%.

2. Pressure transducer calibration error

   The uncertainty of the calibration is due to curve fitting. A first order polynomial was applied to the pressure transducer calibration. The residuals at each calibration point was found and from there the standard deviation (in percentage) was calculated. The *relative standard* uncertainty can be calculated from

$$relative\ standard\ uncertainty = \frac{1}{100}\sigma(\%) \tag{A.1}$$

3. A/D board resolution

   The A/D board resolution error was calculated from,

$$relative\ standard\ uncertainty = \frac{1}{\sqrt{3}}\frac{1}{U}\frac{E_{AD}}{2^m}\frac{\partial U}{\partial E} \tag{A.2}$$

Table A.1: Uncertainties for velocity sample for single probe

Error Source	Relative Standard Uncertainty
Pressure transducer error	0.005
Pressure transducer calibration error	0.005
A/D board resolution	0.0026145
Hot wire calibration error	0.00061

$\frac{\partial U}{\partial E}$ is the slope of the inverse calibration curve. For the A/D board used ($PD2 - MFS - 4 - 2M/14$), $E_{AD} = 10v$, $\frac{\partial U}{\partial E} = 53.42$ and $m = 14$.

4. Hot wire calibration error

   The hot wire calibration error is calculated similar to the calibration error due to the pressure transducer. For the current work, the calibration error is given by the IFA300 system.

   The relative uncertainties are located in Table A.1. The total uncertainties involved are

$2 * \sqrt{0.005^2 + 0.005^2 + 0.0026145^2 + 0.00061^2} = 0.015 = 1.5\%$

   The PIV measurements were taken using a 32 x 32 pixel interrogation window. According to Raffel et all the RMS uncertainty is roughly 0.01 pixels [41]. When data is acquired perpendicular to the flow direction, the uncertainty typically increases by an order of magnitude.

Appendix B

Forcing Mechanism Components

The following Figures were purchased to control the azimuthal forcing mechanism.
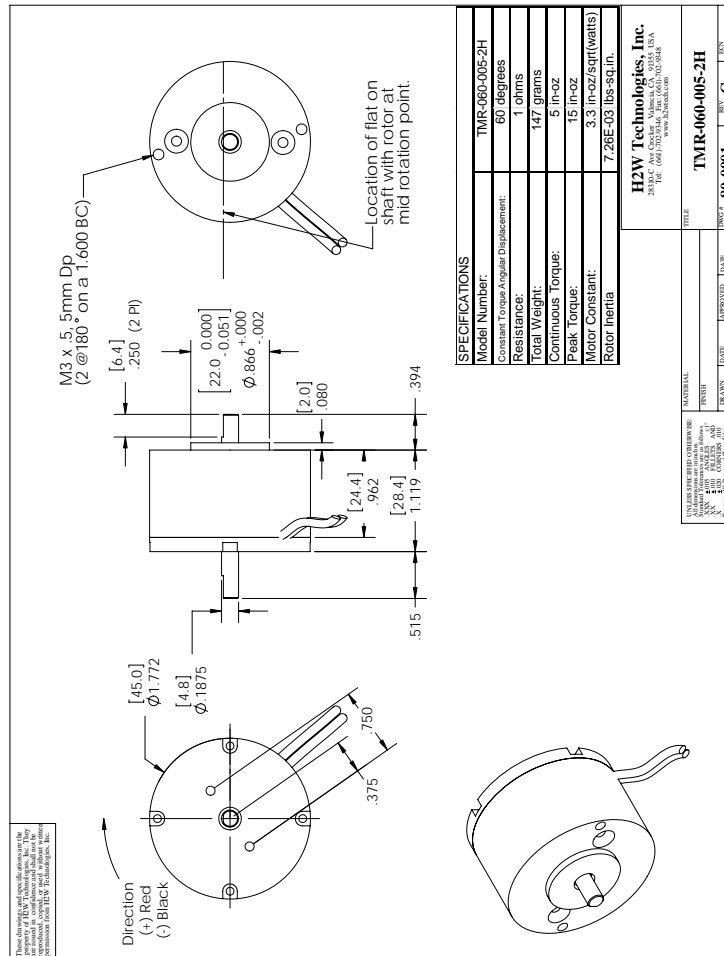
Figure B.1: H2W Limited Angle Torque Motor
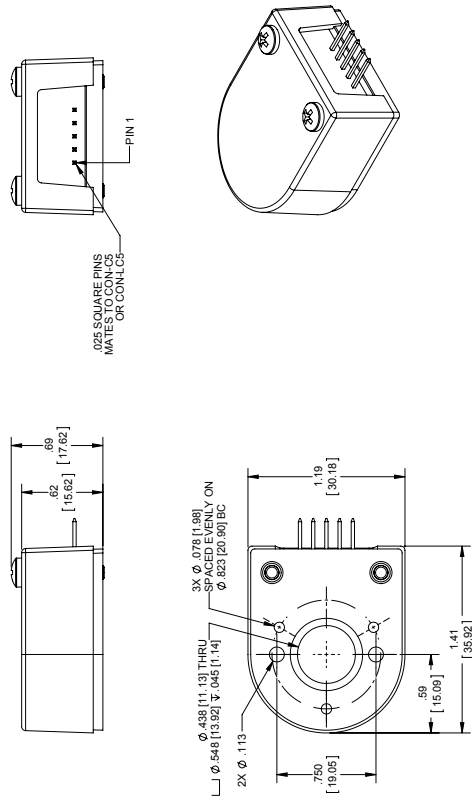
Figure B.2: US Digital Optical Encoder

BLOCK DIAGRAM
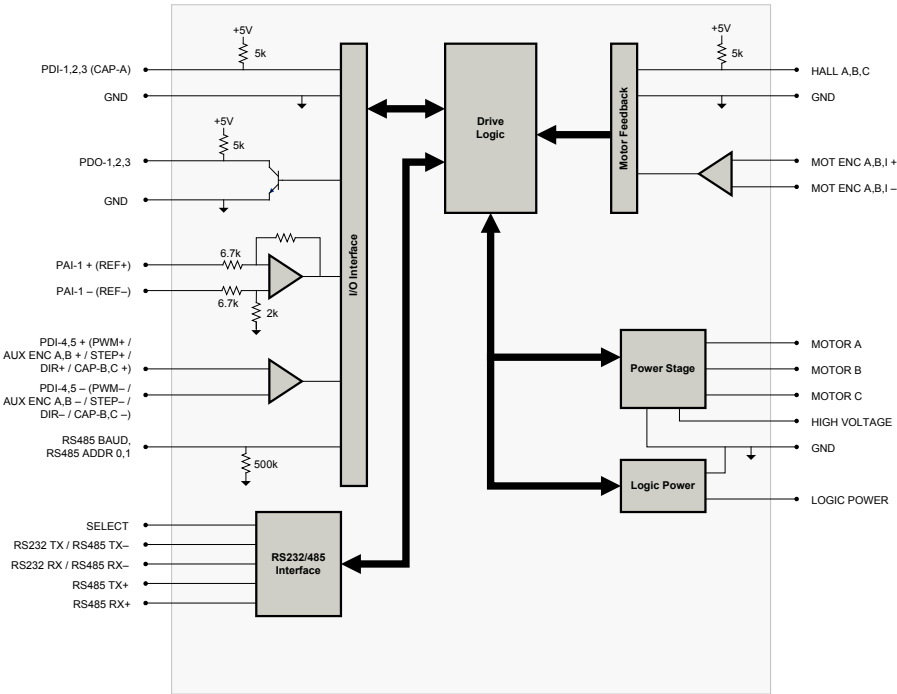
Information on Approvals and Compliances	
cULus	US and Canadian safety compliance with UL 508c, the industrial standard for power conversion electronics. UL registered under file number E140173. Note that machine components compliant with UL are considered UL registered as opposed to UL listed as would be the case for commercial products.
CE	Compliant with European CE for both the Class A EMC Directive 2004/108/EC on Electromagnetic Compatibility (specifically EN 61000-6-4:2007 and EN 61000-6-2:2005) and LVD requirements of directive 2006/95/EC (specifically EN 60204-1:2006), a low voltage directive to protect users from electrical shock.
RoHS COMPLIANCE	RoHS (Reduction of Hazardous Substances) is intended to prevent hazardous substances such as lead from being manufactured in electrical and electronic equipment.

Figure B.3: AMC Servo Motor Block Diagram

55

BLOCK DIAGRAM & SPECIFICATION SUMMARY
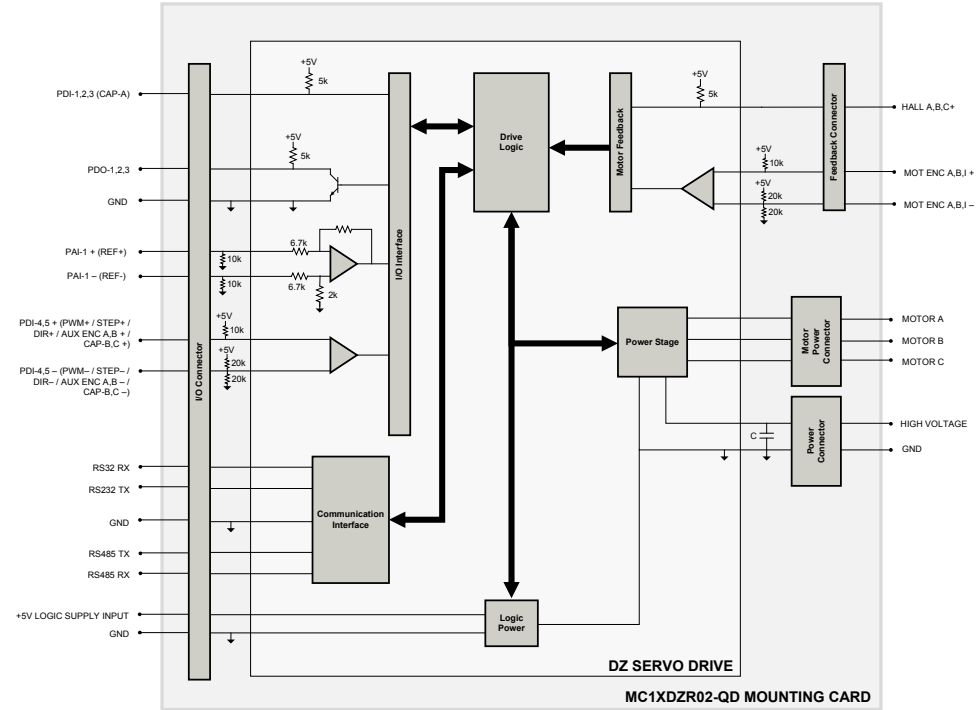
Mechanical Specifications	
Mounting Signal Connector: P1	30-pin, dual-row, 2.54 mm pitch socket
Mounting Power Connector: P2	24-pin, dual-row, 2.54 mm pitch socket
Mounting Power Connector: P3	24-pin, dual-row, 2.54 mm pitch socket
I/O Connector: P4*	16-port, dual-row, 2.00 mm spaced plug terminal
Communication Connector: P5*	10-port, dual-row, 2.00 mm spaced plug terminal
Feedback Connector: P6*	12-port, dual-row, 2.00 mm spaced plug terminal
Motor Power Connector: P7 (mating connector included)	4-port, 5.08 mm spaced insert connector
Power Connector: P8 (mating connector included)	3-port, 5.08 mm spaced insert connector
Bus Capacitance	100 µF / 200 V
Size (L x W x H)	2.5 x 3.0 x 1.0 inches
Weight	50.7 g (1.8 oz)

*Mating Connector Kit

Mating connector housing and crimp pins can be ordered as a kit using *ADVANCED* Motion Controls part number **KC-MC1XDZ02**. This includes mating connector housing and crimp style contacts for the I/O, Feedback, and Communication connectors. The recommended tool for crimping the contacts is Molex part number **63811-6300**.

Figure B.4: AMC Mounting Card Block Diagram

56

Appendix C

Velocity Contour

The following images are the snapshot velocity contours acquired from the PIV analysis of the forced cases.
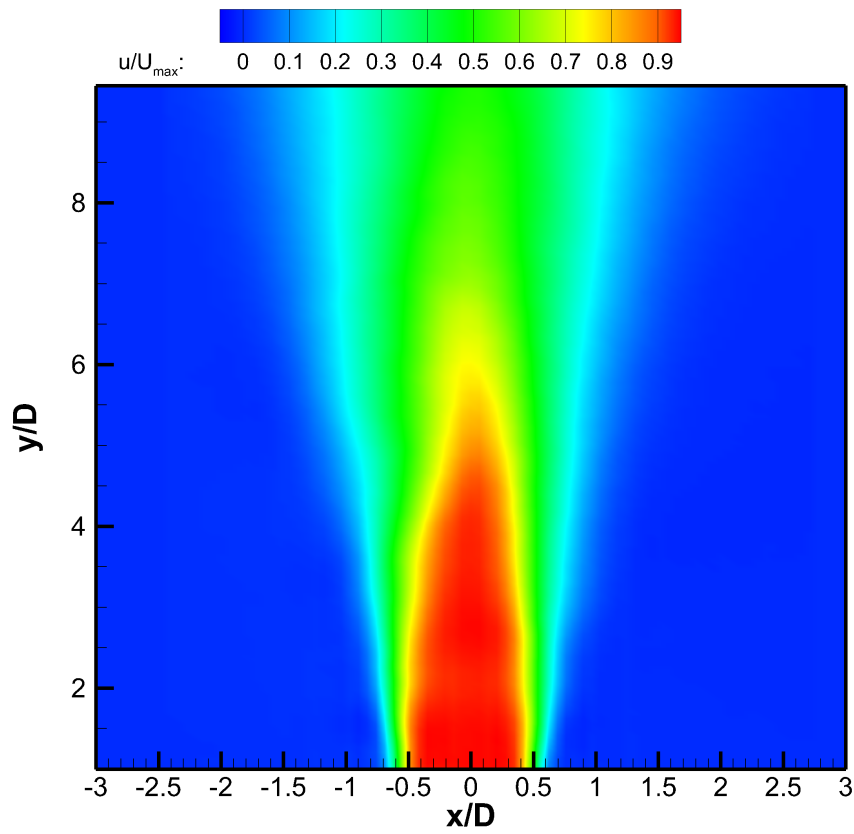
Figure C.1: Velocity Contour, $St = 0.12$
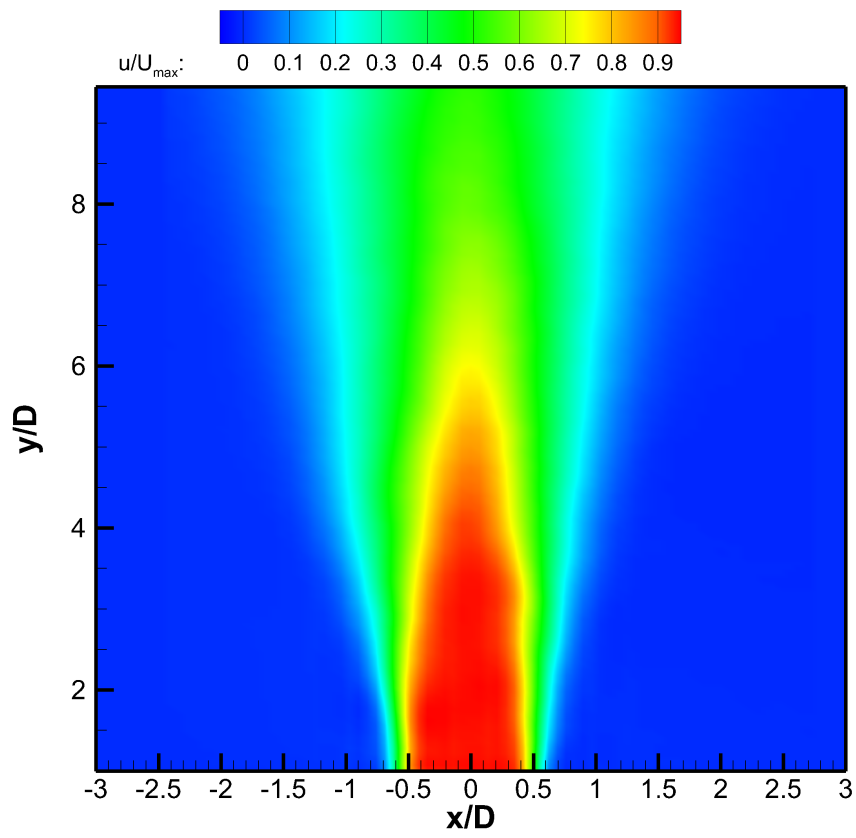
Figure C.2: Velocity Contour, $St = 0.09$

Appendix D

Cross-Spectra
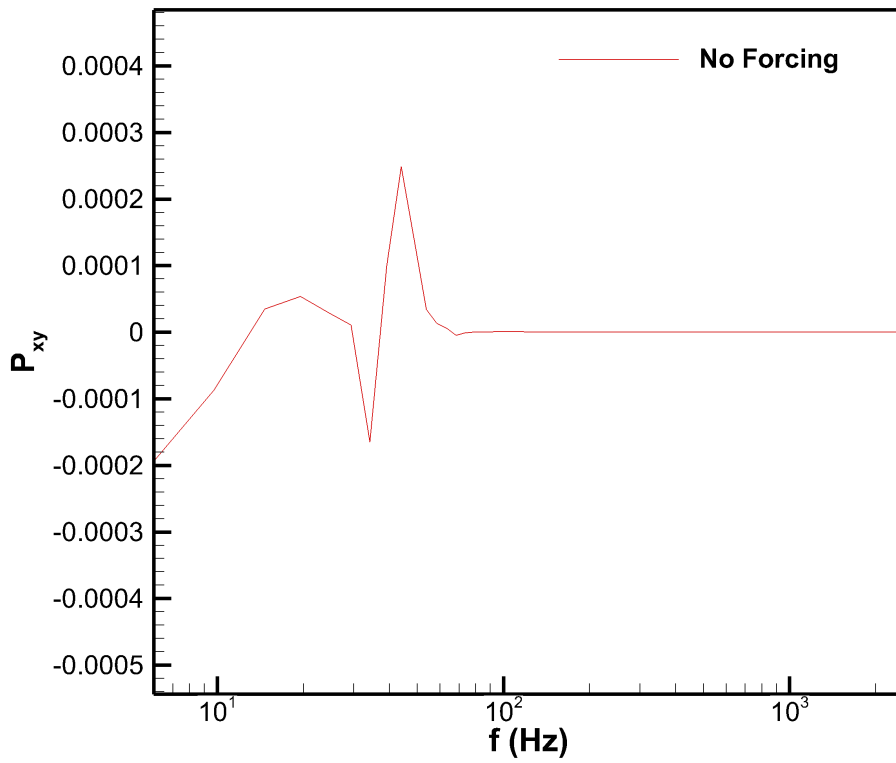
Figure D.1: Cross-Spectra, Unforced
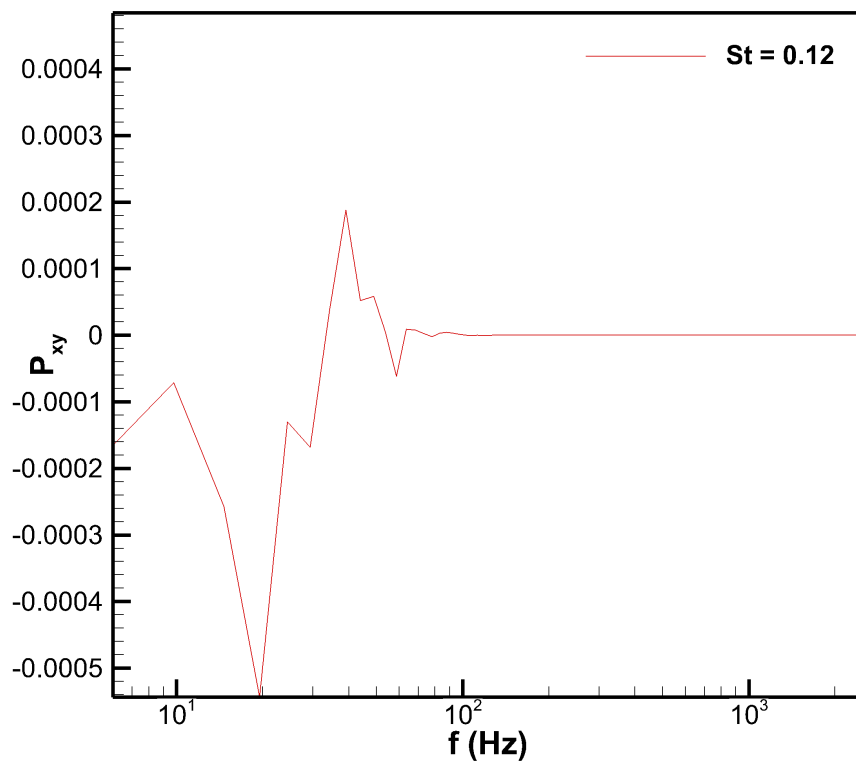
Figure D.2: Cross-Spectra, $St = 0.12$
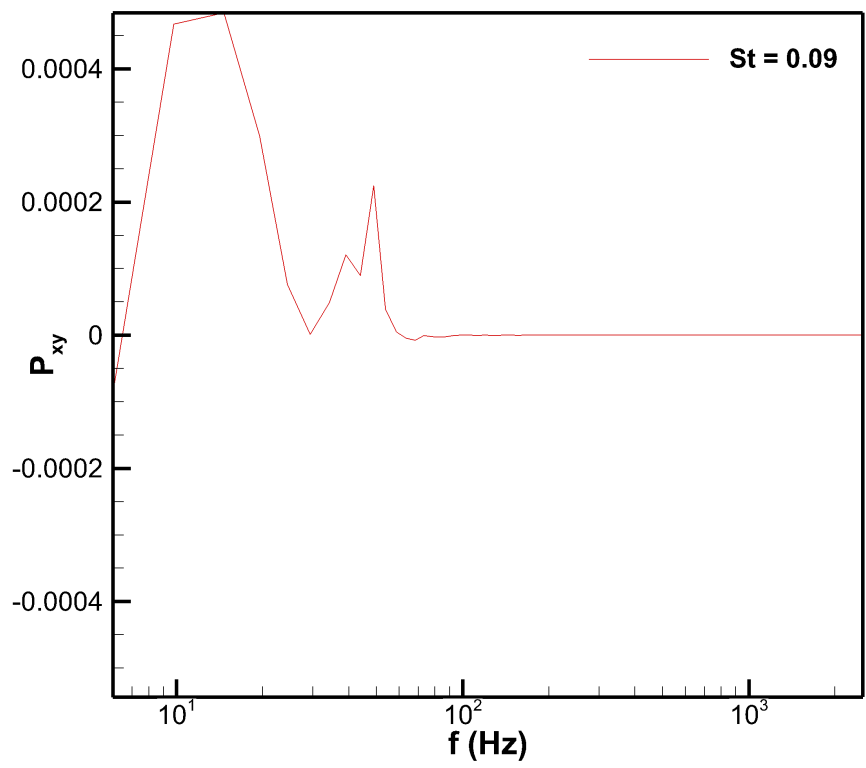
Figure D.3: Cross-Spectra, $St = 0.09$

Appendix E

Mode Distribution
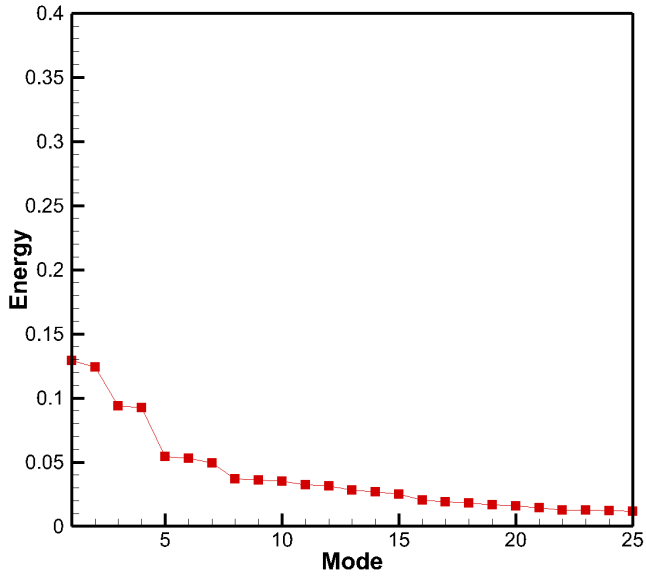
(a) Unforced
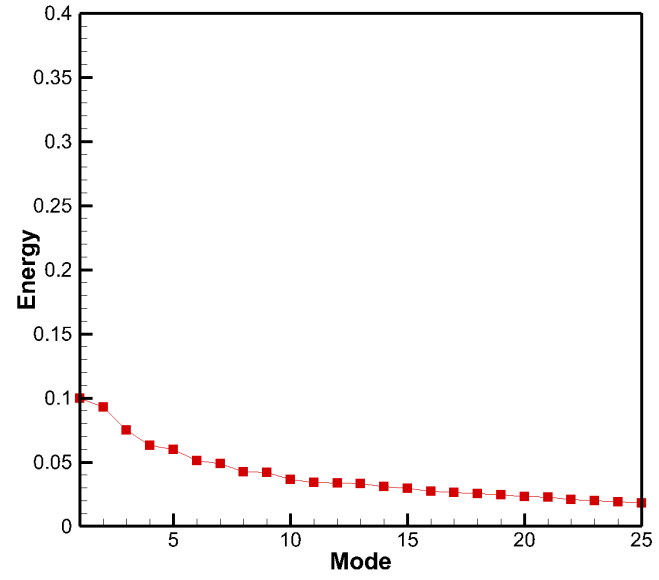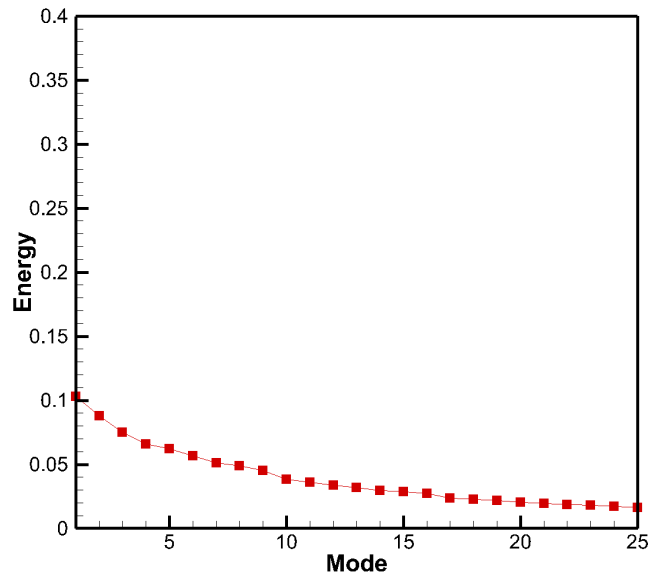
(b) $St = 0.12$

(c) $St = 0.09$

Figure E.1: Energy distribution
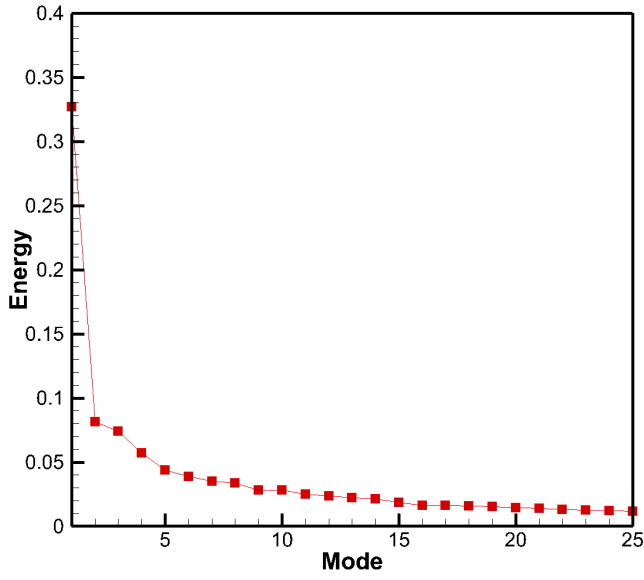
(a) Unforced
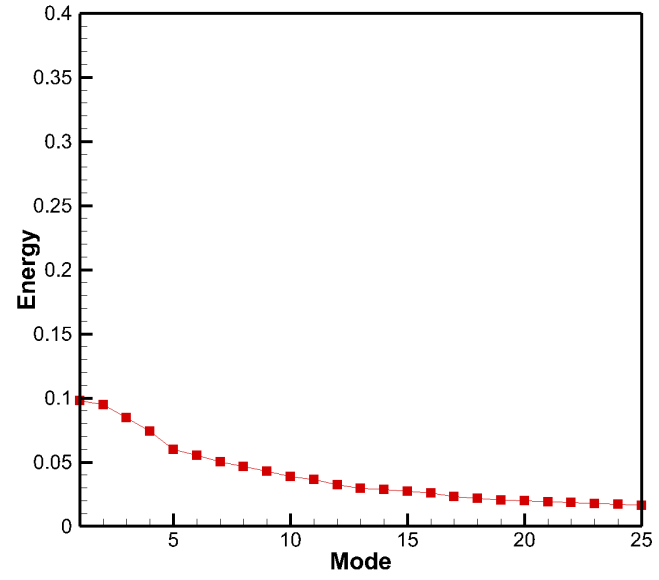
(b) $St = 0.12$
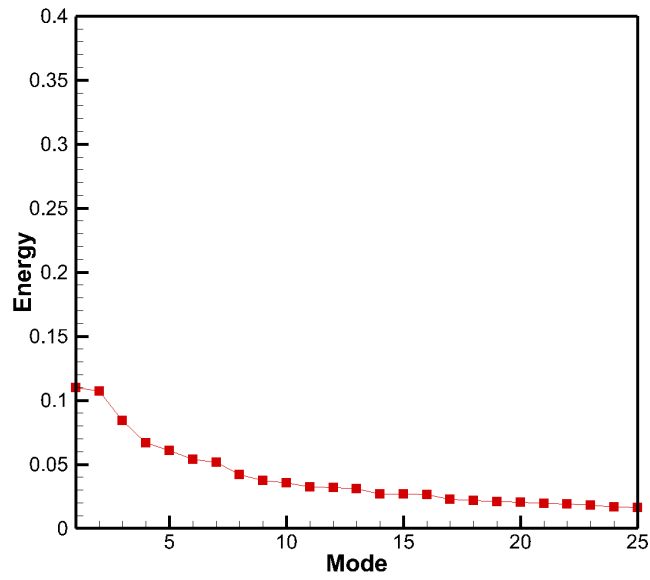
(c) $St = 0.09$

Figure E.2: Energy distribution at $y/D = 4$

Appendix F

Shear layer PSD

Below are additional PSD plots with the CTA probe located within the shear layer at a series of locations downstream.
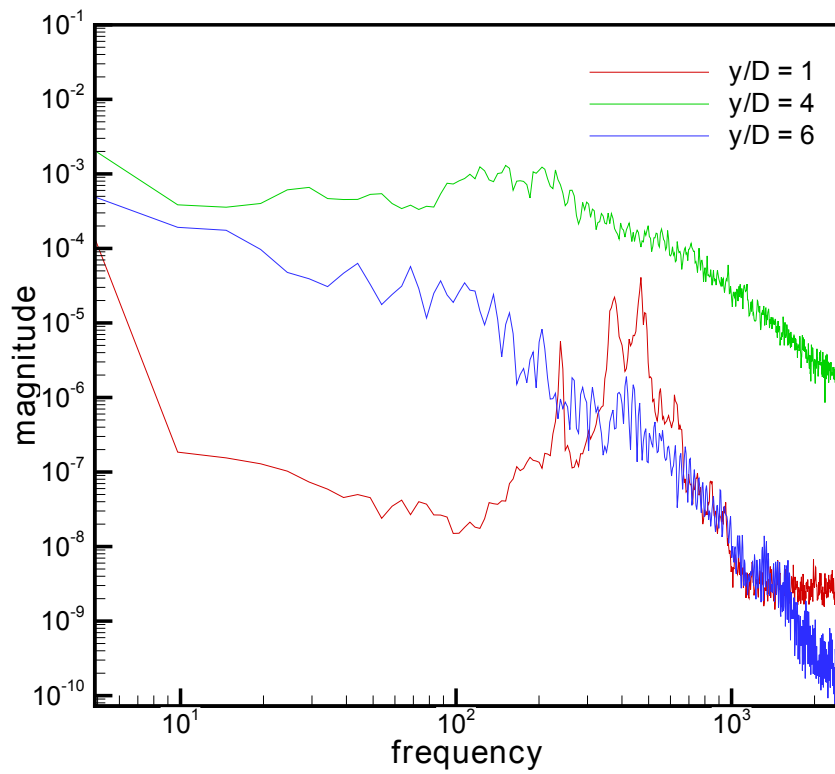
Figure F.1: Shear layer PSD, no forcing
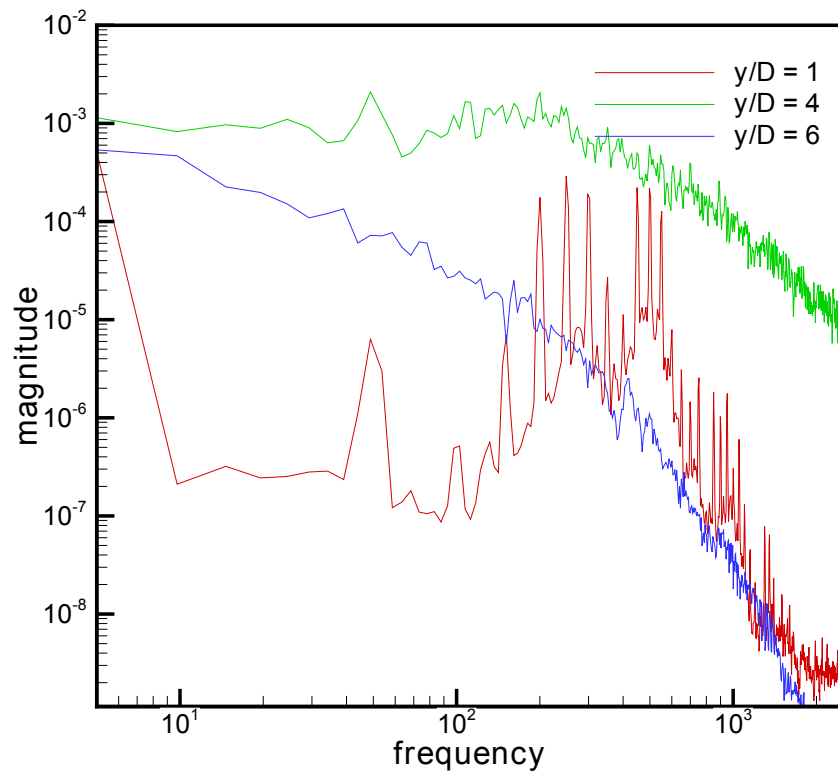
Figure F.2: Shear layer PSD, $St = 0.12$
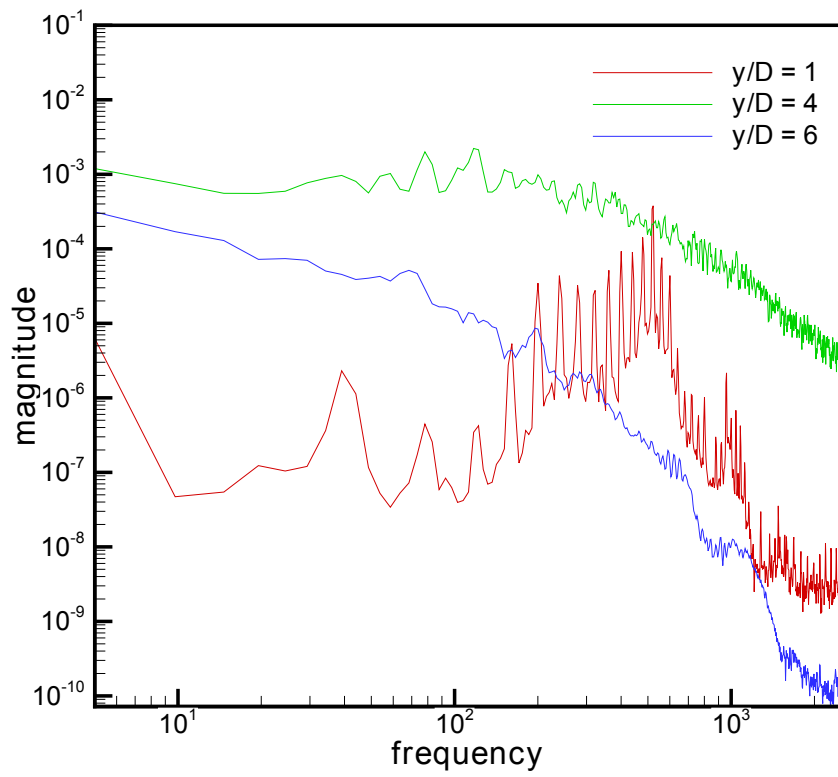
Figure F.3: Shear layer PSD, $St = 0.09$

Appendix G

POD Contour Plots
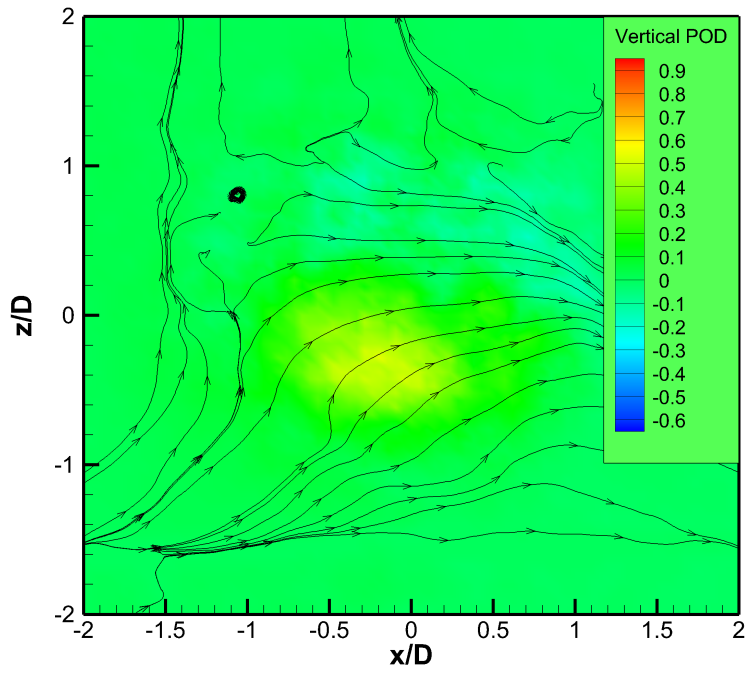
(a) First mode, $St = 0.12$
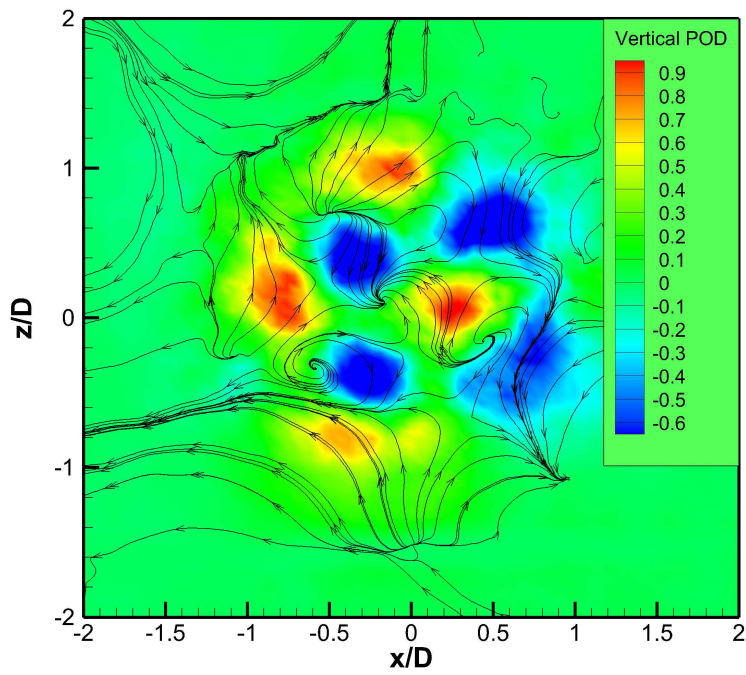
(b) 25^{25} mode, $St = 0.12$

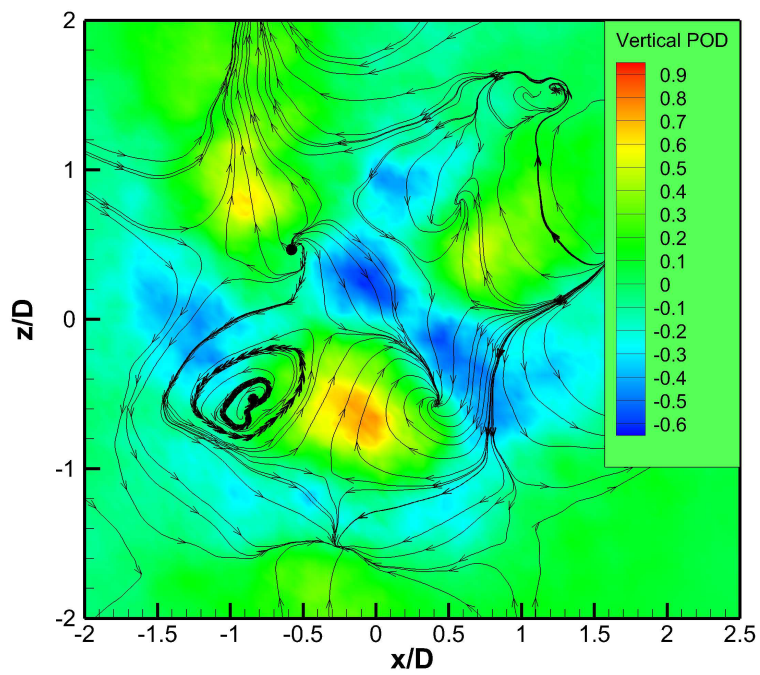Figure G.1: Modal energy for azimuthal cuts at $y/D = 4$ with streamtracers superimposed ($St = 0.12$)
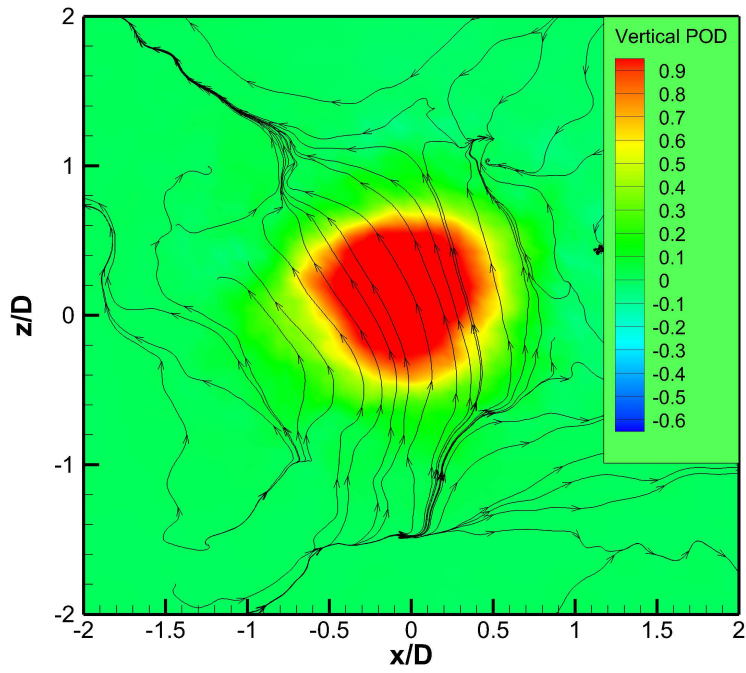
(a) First mode, $St = 0.09$
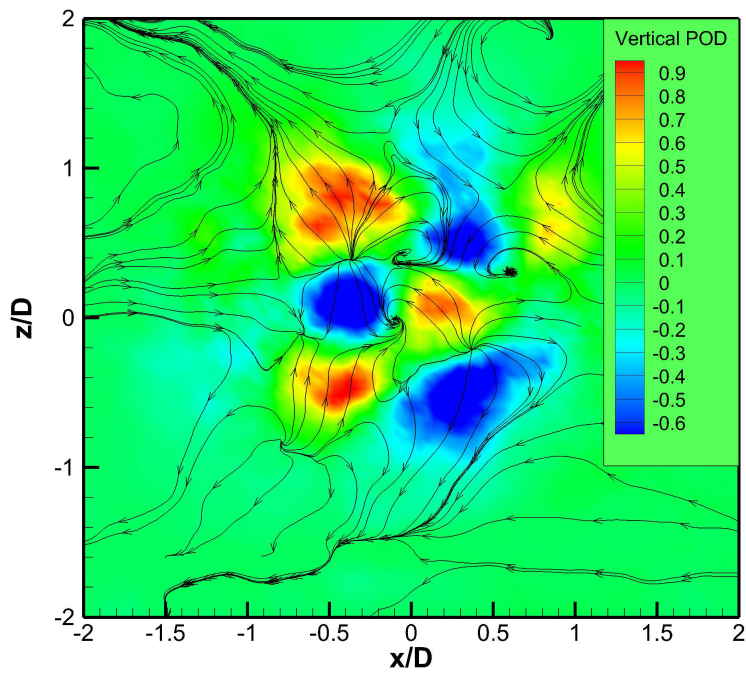
(b) 25th mode, $St = 0.09$

Figure G.2: Modal energy for azimuthal cuts at $y/D = 4$ with streamtracers superimposed ($St = 0.09$)

Figure G.3: No forcing, 25th mode at $y/D = 6$ with streamtracers superimposed
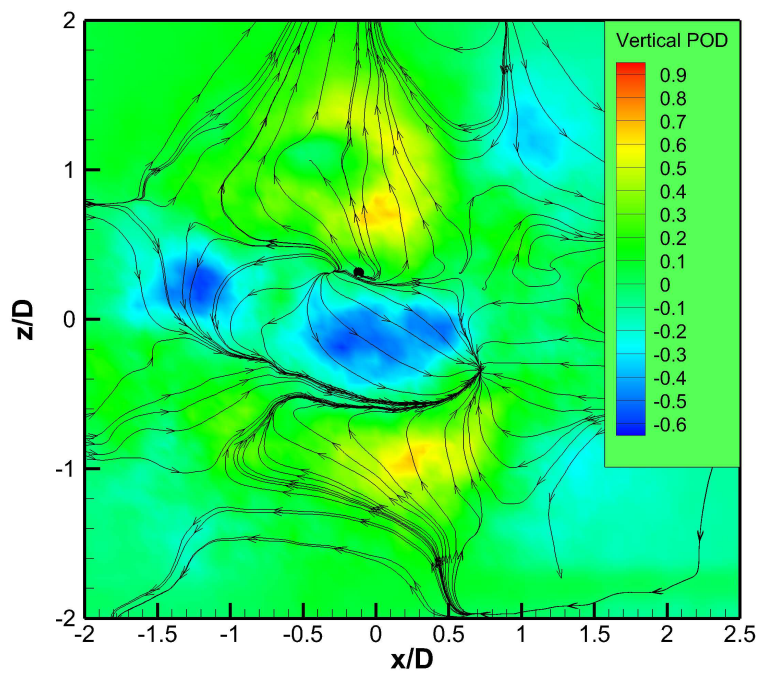
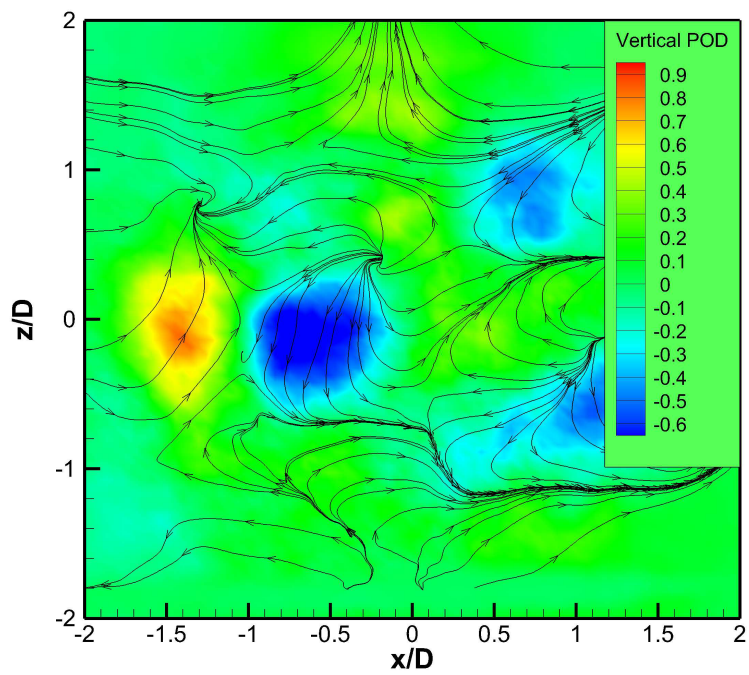Figure G.4: $St = 0.12, 25^{th}$ mode at $y/D = 6$ with streamtracers superimposed

Figure G.5: $St = 0.09, 25^{th}$ mode at $y/D = 6$ with streamtracers superimposed

Appendix H

Turbulent Kinetic Energy

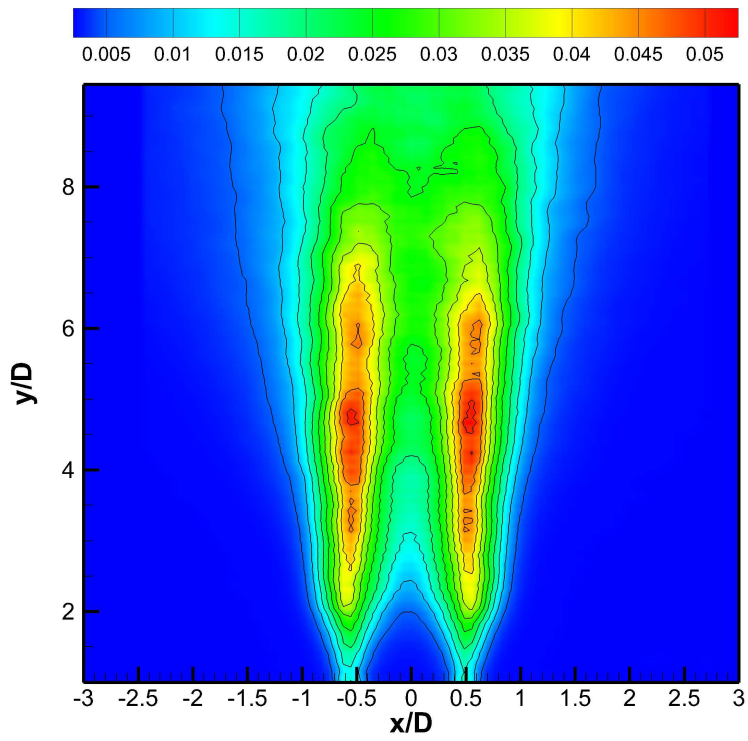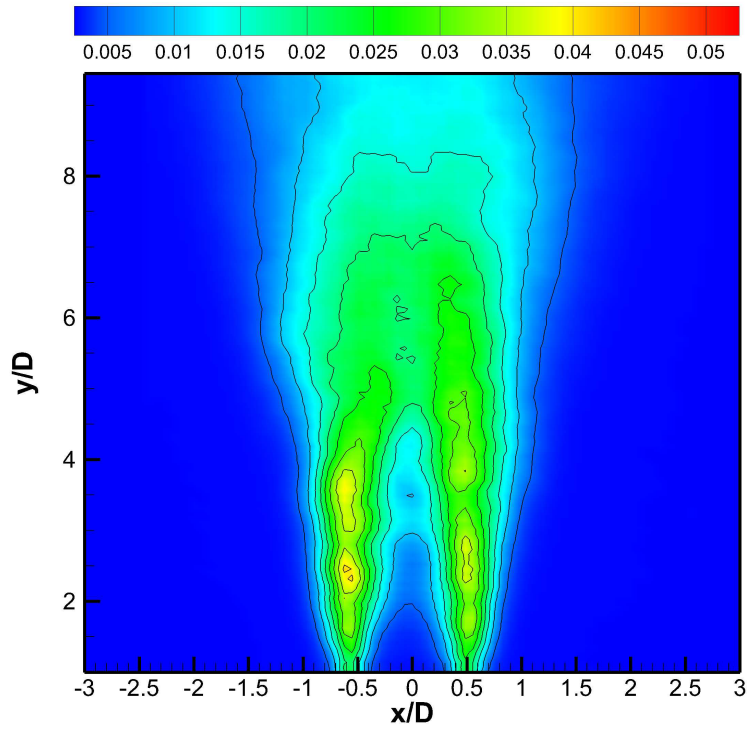Following are similar contour plots of the turbulent kinetic energy with contour lines superimposed.
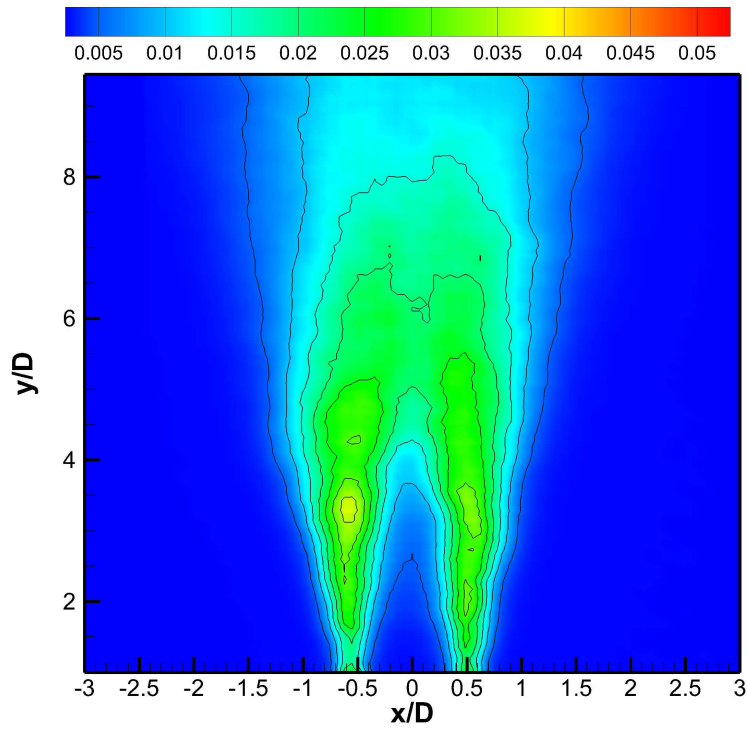

Figure H.1: Turbulent Kinetic Energy for non-forcing

(a) $St = 0.12$

(b) $St = 0.09$

Figure H.2: Turbulent Kinetic Energy for forced cases